SPECIAL OLYMPEX COLLECTION

Observed and Simulated Characteristics of Down-Valley Flow within Stratiform Precipitation over the Olympic Peninsula

ROBERT CONRICK,[a] JOSEPH P. BOOMGARD-ZAGRODNIK,[a] AND LYNN A. MCMURDIE[a]

[a] *Department of Atmospheric Sciences, University of Washington, Seattle, Washington*

(Manuscript received 19 August 2022, in final form 20 February 2023, accepted 22 February 2023)

ABSTRACT: Midlatitude cyclones approaching coastal mountain ranges experience flow modifications on a variety of scales including orographic lift, blocking, mountain waves, and valley flows. During the 2015/16 Olympic Mountain Experiment (OLYMPEX), a pair of scanning ground radars observed precipitating clouds as they were modified by these orographically induced flows. The DOW radar, positioned to scan up the windward Quinault Valley, conducted RHI scans during 285 h of precipitation, 80% of which contained reversed, down-valley flow at lower levels. The existence of down-valley flow in the Quinault Valley was found to be well correlated with upstream flow blocking and the large-scale sea level pressure gradient orientated down the valley. Deep down-valley flow occurred in environments with high moist static stability and southerly winds, conditions that are common in prefrontal sectors of midlatitude cyclones in the coastal Pacific Northwest. Finally, a case study of prolonged down-valley flow in a prefrontal storm sector was simulated to investigate whether latent heat absorption (cooling) contributed to the event. Three experiments were conducted: a Control simulation and two simulations where the temperature tendencies from melting and evaporation were separately turned off. Results indicated that evaporative cooling had a stronger impact on the event's down-valley flow than melting, likely because evaporation occurred within the low-level down-valley flow layer. Through these experiments, we show that evaporation helped prolong down-valley flow for several hours past the time of the event's warm frontal passage.

SIGNIFICANCE STATEMENT: This paper analyzes the characteristics of down-valley flow over the windward Quinault Valley on the Olympic Peninsula of Washington State using data from OLYMPEX, with an emphasis on regional pressure differences and blocking metrics. Results demonstrate that the location of precipitation over the Olympic Peninsula is shifted upstream during events with deep down-valley flow, consistent with blocked upstream airflow. A case study of down-valley flow highlights the role of evaporative cooling to prolong the flow reversal.

KEYWORDS: Coastal flows; Precipitation; Valley/mountain flows; Cloud microphysics; Latent heating/cooling; Mountain meteorology

1. Introduction

Down-valley flow, defined as a localized airflow reversal that acts counter to the mean synoptic-scale wind, has been observed in low-elevation valleys around the world, such as within the Tennessee River valley in the United States (Whiteman and Doran 1993), around the Laggo Maggiore in Italy (Rotunno and Houze 2007), and along windward slopes of the Hawaiian Islands (Carbone et al. 1995, 1998). Early studies on windward slopes of terrain indicated that flow dynamics, specifically stagnation and blocking as air attempts to surmount a barrier, contributed to flow-reversal events (Smith 1980; Smolarkiewicz and Rotunno 1990); however, these studies only considered dry, idealized environments. Later work by Carbone et al. (1995) studied moist airflow over windward slopes of Hawaii and suggested that thermodynamics, particularly the local generation of negative buoyancy by precipitation and precipitation processes, can also contribute to down-valley flow. Later research from the Coastal Observation and Simulation with Topography (COAST; Bond et al. 1997) field experiment over coastal areas of the Pacific Northwest showed that blocked low-level airflow and synoptic-scale wind deflection contributed to down-valley airflow during the prefrontal portion of landfalling midlatitude cyclones (Colle and Mass 1996; Colle et al. 1999).

Down-valley airflow was frequently sampled during the Mesoscale Alpine Programme (MAP), which took place in

Denotes content that is immediately available upon publication as open access.

Corresponding author: Robert Conrick, rconrick@uw.edu and robert.conrick@gmail.com

DOI: 10.1175/MWR-D-22-0229.1

© 2023 American Meteorological Society. For information regarding reuse of this content and general copyright information, consult the AMS Copyright Policy (www.ametsoc.org/PUBSReuseLicenses).

Brought to you by University of Washington Libraries | Unauthenticated | Downloaded 08/28/24 11:35 PM UTC

the Italian Alps during 1999 (Bougeault et al. 2001). While relatively narrow in geographic scope, results from MAP have contributed significantly to the understanding of down-valley flow, though with mixed results on the relative contributions of dynamics and thermodynamics. Steiner et al. (2003) used observational evidence during several down-valley flow events to suggest that while dynamical conditions favored blocking and flow reversal, the confinement of down-valley flow below the melting level and occurrence during precipitation implied a microphysical influence. In one particularly well-documented event (MAP IOP-8), their study showed that down-valley flow began shortly after heavy precipitation was observed. Other studies of IOP-8, however, offered differing interpretations regarding the significance of latent heating/cooling effects. For example, Bousquet and Smull (2003) concluded that dynamically induced flow blocking was the phenomenon's primary driver with cooling from microphysical processes a secondary contributor.

Simulations from mesoscale models have proven useful in understanding down-valley flow and the relative roles of dynamics and thermodynamics. Two complementary studies, Asencio and Stein (2006) and Zängl (2007) both investigated the MAP IOP-8 event studied by Steiner et al. (2003) and Bousquet and Smull (2003). Their results agreed that dynamics and thermodynamics both contributed to down-valley flow, though Asencio and Stein (2006) found a much stronger influence from latent heating effects than Zängl (2007). The results from these studies, however, do appear to be case dependent. Asencio and Stein (2006) simulated an additional event, MAP IOP-3, and found that down-valley airflow during the event was influenced nearly exclusively by blocked flow rather than latent heating effects. Other studies, such as Thériault et al. (2012, 2015) found that melting snow in the lower atmosphere contributed significantly to down-valley airflow within a valley near Vancouver, Canada by altering low-level stability. Later work by Conrick et al. (2018) over the Olympic Mountains of Washington State showed that flow blocking and terrain interactions were associated with down-valley flow in some cases, but the large-scale pressure difference played a significant role in others.

Alongside the implications for airflow and temperature, precipitation may also be affected by down-valley flow and its coincident conditions. James and Houze (2005) showed that blocked flow conditions resulted in greater aerial coverage of offshore precipitation than unblocked conditions over California. Bousquet and Smull (2003) and Rotunno and Ferretti (2003) similarly highlighted that periods of down-valley flow tended to have greater upstream precipitation enhancement, which they attributed to flow blocking, a finding also implied by Zagrodnik et al. (2019). Down-valley flow may also affect precipitation intensity and distribution. Medina and Houze (2016), Barnes et al. (2018), and Conrick et al. (2018) all demonstrated the significance of down-valley flow for developing strong shear zones leading to Kelvin–Helmholtz waves, which in turn were shown to modify precipitation microphysics. Despite these studies investigating the links between precipitation and down-valley airflows, additional work is needed to determine the influence of down-valley flow on precipitation patterns.

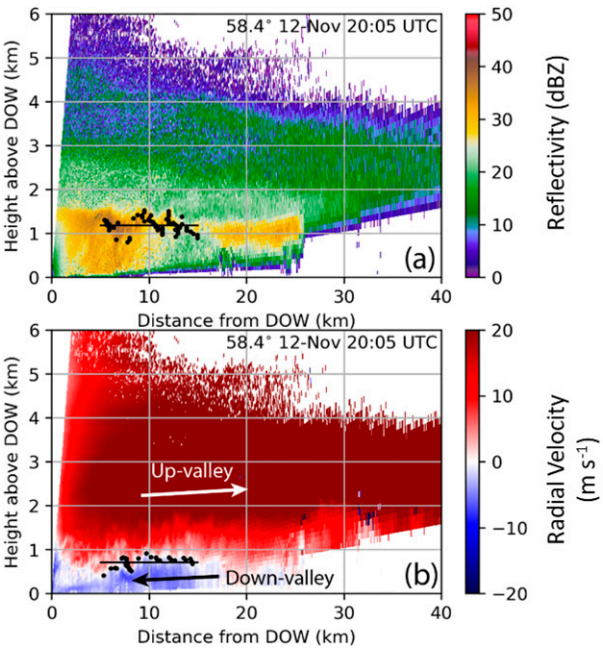

FIG. 1. An example RHI scan at 2005 UTC 12 Nov 2015 from the DOW radar's 58.4° RHI scanning within the Quinault Valley toward the northeast (see Fig. 2 for location). (a) Reflectivity and (b) radial velocity, with arrows highlighting the up- and down-valley flow present during this time. The black dots and horizontal lines represent the melting level in (a) and the down-valley flow detection algorithm in (b).

The purpose of this study is to understand down-valley airflows, their associated precipitation patterns, and sensitivities to latent heating/cooling within the windward Quinault Valley of the Olympic Mountains of Washington State, an area that has received little attention in this regard. The Olympic Mountains were the location of the 2015/16 Olympic Mountains Experiment (OLYMPEX; Houze et al. 2017), which resulted in a vast collection of surface-based microphysical, precipitation, and radar observations during midlatitude cyclones.

For this study, we define down-valley flow as a low-level airflow reversal which is acting counter to the mean synoptic-scale wind. During OLYMPEX, such low-level flow reversals consisted of offshore-directed wind at low levels below onshore wind at higher altitudes. Figure 1 shows an example of down-valley airflow within the Quinault Valley as sampled by a mobile radar on 12 November 2015, during OLYMPEX. Strong ~1-km-deep down-valley airflow occurred at low levels from 0 to 15 km from the radar, with a sharp transition to up-valley flow above 1 km. Such conditions were commonly observed in the valley and reported by OLYMPEX campaign personnel during the winter of 2015/16.

This study aims to classify and analyze OLYMPEX radar observations from the Quinault Valley during the November 2015 to January 2016 period with the goal of better understanding down-valley flow in the region. By comparing radar observations against reanalysis data and measurements from rain gauges, we analyze the conditions coincident with down-valley

Brought to you by University of Washington Libraries | Unauthenticated | Downloaded 08/28/24 11:35 PM UTC

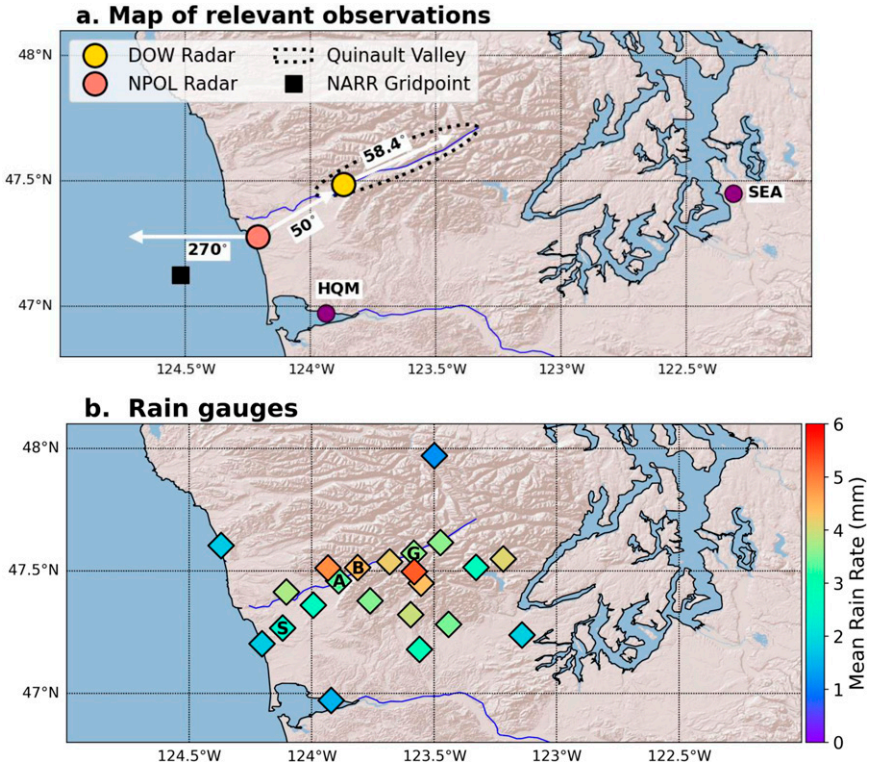

FIG. 2. (a) A map of the Olympic Peninsula and surrounding areas with the locations of the NPOL and DOW radars marked. The white arrows represent the RHI scans used in this study. SEA and HQM are the locations of the Seattle, WA, and Hoquiam, WA, ASOS sites, respectively. (b) Locations of rain gauges within and adjacent to the Quinault Valley. Lake Quinault, where the DOW was located, is near the center of the map. In (b), the letters S, A, B, and G correspond to the Seed Orchard, Amanda Park, Bishop Field, and Graves Creek, respectively, which are referenced in section 4. Marker colors indicate the mean rain rate at each station over the 285 h of observations.

flow and the resultant precipitation patterns. Finally, a case study of prolonged down-valley flow, 16–17 November 2015 is simulated to examine the relative roles of dynamics and thermodynamics, with particular emphasis on the role of cooling from evaporation and melting processes. The following questions are addressed in the study:

1) What are the origins and conditions associated with down-valley flow periods in the Quinault Valley?
2) What precipitation patterns are associated with down-valley flow over the region?
3) What are the relative contributions of dynamics and thermodynamics to down-valley flow during the 16–17 November 2015 event?

2. Methodology, observations, and data

Data for this study are from the Olympic Mountains Experiment (OLYMPEX), which took place during the autumn and winter of 2015/16 (November 2015–January 2016). The goal of OLYMPEX was to provide ground validation for the Global Precipitation Measurement Mission satellite (GPM; Hou et al. 2014; Skofronick-Jackson et al. 2017) and collect microphysical observations critical for understanding precipitation over midlatitude coastal terrain (Houze et al. 2017). The observation period consisted of more than two dozen midlatitude frontal systems that impacted the Olympic Mountains (Houze et al. 2017). Total precipitation during the campaign was nearly 150% of normal within the windward Quinault Valley.

To understand down-valley flow in the Quinault Valley of western Washington State and its implications for precipitation, this study uses a variety of OLYMPEX and routine weather observations from around the Olympic Peninsula (Fig. 2). Central to our analysis of down-valley flow is the NASA S-Band Dual-Polarimetric Radar (NPOL; Wolff et al. 2017), which was located on an approximately 150-m coastal bluff on the southwestern end of the peninsula. The NPOL radar scanned an offshore sector to sample incoming storms and an onshore sector that sampled precipitation within the Quinault Valley and surrounding terrain. In addition to Plan Position Indicator (PPI) scans,[1] the

[1] PPI scans have a constant elevation angle and variable azimuth angle. Radar returns are then mapped to a horizontal plane. During OLYMPEX, NPOL produced PPI surveillance scans (azimuth: 0°–360°).

Brought to you by University of Washington Libraries | Unauthenticated | Downloaded 08/28/24 11:35 PM UTC

NPOL radar routinely produced Range Height Indicator (RHI) scans[2] both offshore and within the Quinault Valley. Another radar, the X-band Doppler-on-Wheels (DOW; Houze et al. 2018) was located within the Quinault Valley on the shores of Lake Quinault. The DOW was positioned to scan up the valley toward the northeast. The DOW exclusively produced RHI scans during the campaign, helping to provide essential data at levels below the lowest altitude that NPOL sampled. From the NPOL radar, we used the 270° (west) and 50° (northeast) RHI scans. The 270° azimuth allows for offshore flow to be sampled, while the 50° RHI offers information regarding airflow between the coast and the mouth of the valley. From the DOW radar, the 58.4° RHI azimuth was analyzed, allowing airflow within the valley to be sampled. Both the 50°NPOL and 58.4° DOW azimuth were chosen to minimize terrain blockage by the 1–1.5-km-tall mountain ridges on either side of the Quinault Valley.

To identify down-valley flow, we built a simple algorithm to detect the occurrence of flow reversals in the Doppler velocity data. A single DOW RHI azimuth consists of 287 rays at varying elevation angles from 0° to 90°. Each ray consists of 781 gates representing the return of each radar pulse along a line with increasing horizontal (x) and vertical (z) distance from the radar. As demonstrated in Fig. 1, when down-valley flow and precipitation are occurring concurrently, the Doppler velocity returns from a scan pointing up the valley will abruptly switch from negative velocity (down-valley flow toward the radar) to positive velocity (up-valley flow away from the radar) at various (x, z) locations from the radar.

Our algorithm examines each ray in the RHI scan and finds the (x, z) coordinates of the transition from down-valley to up-valley flow. Several procedures are implemented to mitigate the impact of noise, clutter, and turbulence at the top of the down-valley flow layer. First, we smooth Doppler velocity data along each ray with a five-gate rolling average. Second, we set several thresholds including a specified minimum reflectivity near the transition location (10 dBZ), three fixed ranges (5–15 km from DOW; 5–15 km onshore for NPOL, and 45–55 km offshore for NPOL) from the radars to search for flow reversals, which were chosen to be close enough to ensure optimal radar coverage while also minimizing clutter and noise, and a minimum requirement of successful flow reversal detection along at least 10 consecutive rays in the specified x range. An example of the retrieved DOW flow-reversal locations is shown as black dots in Fig. 1b. We considered the down-valley flow height to be the average height of the detected reversal points, shown by a black horizontal line in Fig. 1b.

The hourly down-valley flow height was computed by averaging the radar-retrieved flow reversal height at all scans within each hour, which is usually 12 scans per hour for DOW and 3 scans per hour for NPOL. The dataset was further restricted to hours when at least 1 mm of precipitation was recorded at the Bishop Field site near DOW. This resulted in 285 h of data over the period from 13 November 2015 to 15 January 2016. The height (depth) of the down-valley flow was chosen for analysis, rather than velocity, due to 1) the presence of turbulence at the interface between down- and up-valley flow, which occasionally manifested as Kelvin-Helmholtz waves; and 2) ground clutter within the complex terrain of the valley, resulting in poor velocity estimates during shallow flow reversals.

Alongside the radars positioned within the Quinault Valley, 21 tipping-bucket rain gauges provided precipitation data. Gauges were distributed within and in the vicinity of the Quinault Valley (Fig. 2b) and are used to understand how precipitation varies during down-valley flow periods. More information about these gauges can be found in Petersen et al. (2017) and Zagrodnik et al. (2018).

To understand the synoptic conditions that support down-valley flow, we also used sea level pressure (SLP) measurements from National Weather Service (NWS)/Federal Aviation Administration (FAA) Automated Surface Observing Stations (ASOS) at Hoquiam, WA (HQM), and Seattle, WA (SEA), the locations of which shown in Fig. 2b. Moist static stability (moist Brunt–Väisälä frequency N_m^2; Durran and Klemp 1982) and wind characteristics (direction and speed) were retrieved from the North American Regional Reanalysis (NARR; Mesinger et al. 2006) reanalysis dataset at the grid point closest to the NPOL radar, which is upwind of the Quinault Valley. Because the soundings launched at NPOL were not launched on a regular schedule and the routine launches at Quillayute, Washington (KUIL), are only every 12 h, we opt to use reanalysis because it provides greater temporal resolution without the need for extensive interpolation.

3. Statistics of down-valley flow during OLYMPEX

From 12 November 2015 to 15 January 2016, 285 h of precipitation were sampled by radars within and in the vicinity of the Quinault Valley. Of those 285 h, 20% (57 h) had no down-valley (reversed) flow detected. The remaining 228 h serve as the basis for our analysis of down-valley flow in the Quinault Valley.

The 228 h of data were divided into three distinct flow regimes based on their vertical and horizontal extent along the valley. The most frequent type, defined by deep (>500 m) down-valley flow extending offshore, occurred during 97 of the 228 h of down-valley flow (42%). The second most frequent type of flow identified was deep (>500 m) down-valley flow not reaching the coast, occurring 74 of the 228 h (32%). Finally, shallow (<500 m) down-valley flow occurred 25% of the time (57 h). Figure 3 shows example radar RHI scans of Doppler velocity for each type of down-valley flow.

a. *Environments that favor down-valley flow*

To explore the mechanisms which promoted down-valley flow in the Quinault Valley, we consider the Seattle-to-Hoquiam (SEA–HQM) pressure difference, the 925- and 850-hPa wind direction and speed, low-level moist static stability (moist Brunt–Väisälä frequency N_m^2), and the nondimensional mountain height (M; defined shortly). The SEA–HQM pressure difference serves as an indicator of the synoptic-scale pressure gradient along the long axis of the valley, and the low-level wind

[2] RHI scans have a constant azimuth angle and variable elevation angles. Radar returns are mapped to a vertical plane. During OLYMPEX, both NPOL and DOW produced RHIs at different azimuths. See Houze et al. (2017).

Brought to you by University of Washington Libraries | Unauthenticated | Downloaded 08/28/24 11:35 PM UTC

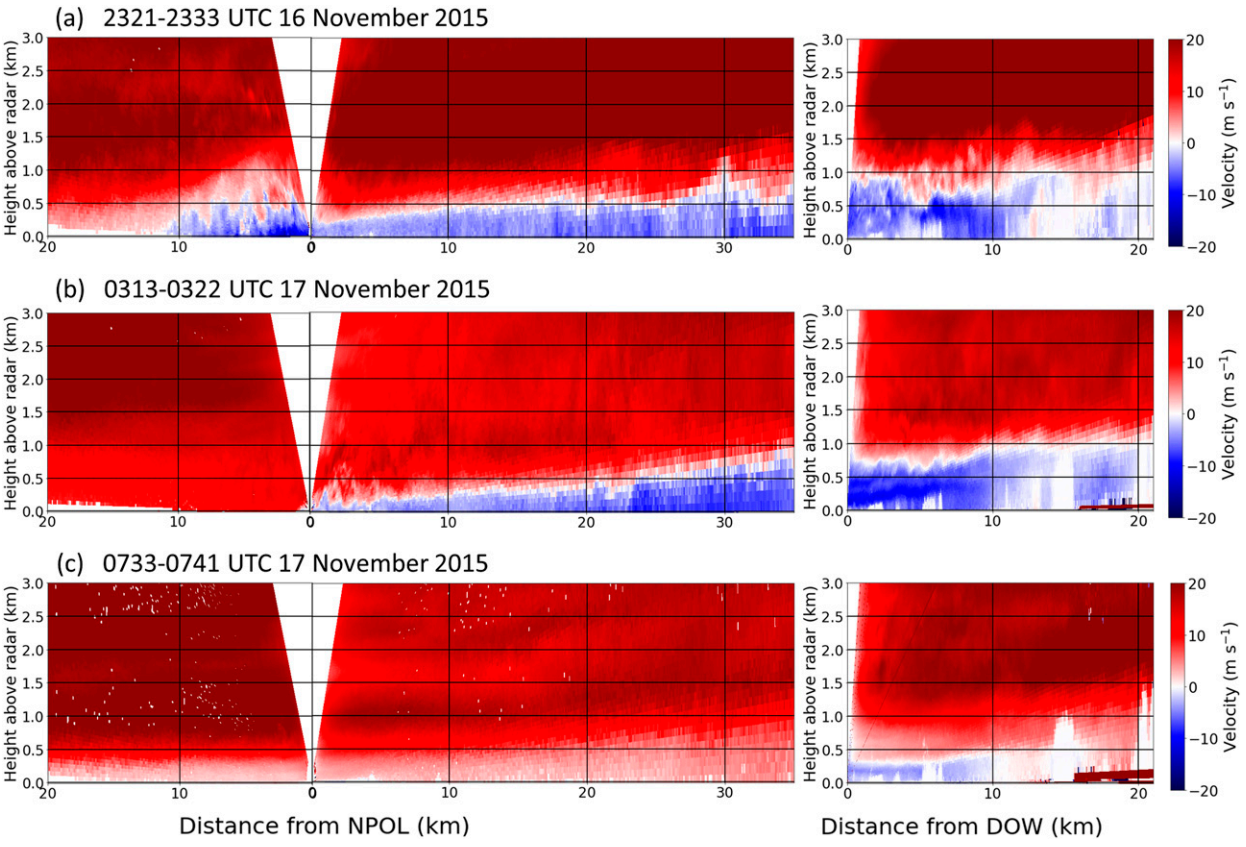

FIG. 3. Example RHI scans from the 16–17 Nov 2015 down-valley flow event. Data are obtained from RHI scans within or immediately upstream of the Quinault Valley. Examples of (a) deep flow extending offshore, (b) deep flow not extending offshore, and (c) shallow down-valley flow. (left) RHIs from NPOL and (right) RHIs from the DOW. Negative (blue) velocities are down-valley wind. The cross sections shown are produced by combining (left) the offshore NPOL RHI (270°), (center) the onshore NPOL RHI (50°), and (right) the up-valley DOW RHI (58.4°).

and stability measures are necessary to understand the contributions of low-level blocking and deflection, the importance of which is roughly quantified by the nondimensional mountain height. Appendix A provides summary statistics for all metrics for each down-valley flow category, including hours when no reversed flow was detected.

The SEA–HQM pressure difference, which can be considered as a driver of large-scale near-surface airflow around and within the Quinault Valley as well as a proxy for the relative strength and position of synoptic-scale fronts passing over the Olympic Peninsula, was positive (offshore) during 69.9% of all analyzed hours and was moderately correlated with the depth of down-valley flow ($r = 0.44$; Fig. 4a). In the context of the flow classifications introduced earlier, deep (>500 m) down-valley flow that extended offshore occurred almost exclusively during strong positive pressure differences (median: 2.7 hPa) and deep flow not reaching the coast occurred during more moderate positive pressure differences (median: 1.9 hPa). Shallow down-valley flows were observed in a large range of values from −3 to 4 hPa, resulting in a median pressure difference near zero (0.04 hPa). Finally, nonexistent down-valley flows were generally associated with negative (onshore) SEA–HQM pressure differences (median: −0.87 hPa). To illustrate this, Fig. 4a shows the classifications as a function of down-valley flow depth and the SEA–HQM pressure difference.

Several past studies have highlighted the importance of flow blocking and deflection for the development and maintenance of down-valley flow, with many considering blocked flow upwind of a topographic barrier as a key contributor to airflow reversals in valleys (e.g., Whiteman and Doran 1993; Carbone et al. 1995; Steiner et al. 2003). To investigate this, we consider the moist nondimensional mountain height, a metric widely used to diagnose the presence of topographic flow blocking (Smith 1980; Jiang 2003; Reinecke and Durran 2008). The moist nondimensional mountain height (M; hereafter referred to as the nondimensional mountain height) is defined as

$$M = \frac{N_m h}{U},$$

where N_m is the square root of the upstream moist Brunt–Väisälä frequency,[3] h is the height of the topographic barrier,

[3] The use of N_m^2 assumes saturated flow, which results in underestimated flow stability and, by extension, M, if the atmosphere is not fully saturated.

Brought to you by University of Washington Libraries | Unauthenticated | Downloaded 08/28/24 11:35 PM UTC

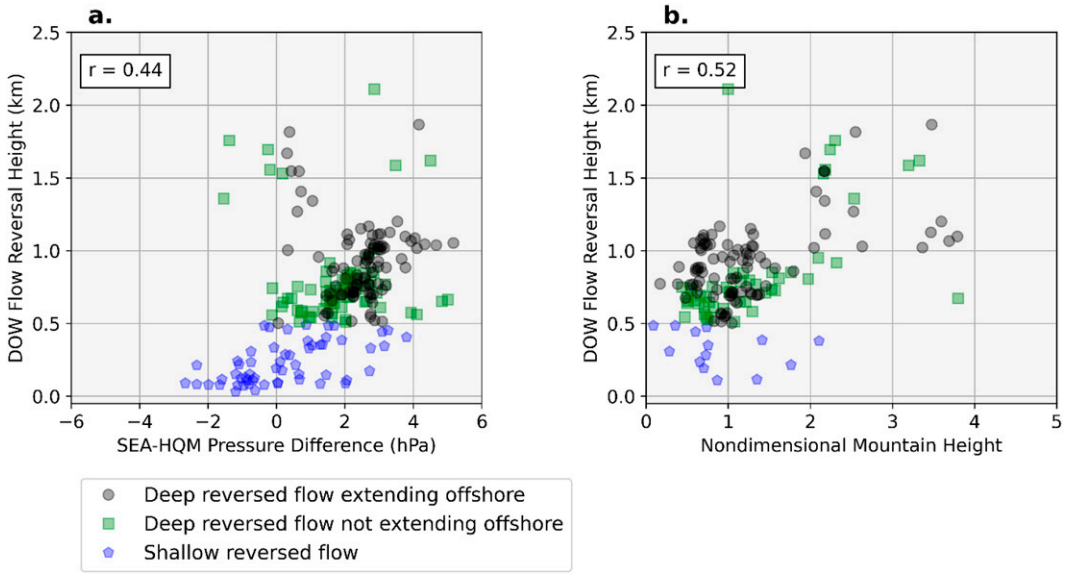

FIG. 4. (a) SEA–HQM pressure difference and (b) the nondimensional mountain height vs the flow reversal height over the DOW radar. Icon shapes and colors correspond to the different classes of down-valley flow defined at the beginning of section 3. Each icon represents 1 h of observed down-valley airflow.

and U is the upstream wind speed. For our calculation of M, we set h to be 2500 m, which is the approximate maximum height of the Olympic Mountains; U is the 0–2500-m mean wind speed projected along the long axis of the valley and N_m is also the average over the 0–2500-m layer. Values of U and N_m are taken from a NARR data point close to the NPOL radar, as shown in Fig. 2a. The NPOL radar is approximately 40 km upstream from the DOW radar where the down-valley flow depth is computed. Despite being taken from a NARR grid point over the ocean, we acknowledge that the lowest few hundred meters of the U and N_m profiles may be affected by flow reversals or low-level inversions. While interpretation of M is complicated by nonuniform vertical distributions of N_m and U as well as the dome-shaped topography of the Olympic Mountains, increasing values of M indicate that airflow blocking is becoming increasingly likely upstream of a barrier. For a given h, larger values of M are a result of 1) increased stability and 2) decreased wind speed upstream of the barrier.

The depth of down-valley flow was well-correlated with M ($r = 0.52$) indicating that deeper down-valley flow events were more likely to be associated with upstream environments that favored topographic flow blocking and/or deflection (Fig. 4b). Median values of M were 1.04 during deep down-valley flow that extended offshore, 1.07 when deep down-valley flow did not extend offshore, and 0.73 during shallow down-valley flow events. It is important to note that M is not defined when N_m^2 is negative (unstable), and therefore 75.4% ($n = 43$) of shallow events and 16.9% ($n = 29$) of deep events do not have a value of M associated with them. Moreover, the overwhelming majority (87.5%) of hours with $M > 0$ occurred when the SEA–HQM pressure difference was positive (offshore), yet no relationship existed between these two metrics ($r = 0.044$, not shown). One explanation for this lack of correlation is that the degree of blocking is not necessarily related to the timing or strength of synoptic-scale frontal passages.

As an aside, while blocked flow will contribute terrain-induced mesoscale pressure perturbations to the SEA–HQM pressure difference, previous studies such as Mass and Ferber (1990) have shown that such contributions tend to be less than 0.6 hPa during environments associated with down-valley flow. Such a small contribution to the overall SEA–HQM pressure difference, compared to pressure differences shown in Fig. 4a, would likely not significantly alter our results. Moreover, there are insufficient routine pressure observations around the Olympic Peninsula to elucidate such mesoscale contributions from the dataset we consider.

To further investigate down-valley flow in the Quinault Valley and its relationship to flow blocking or other environmental factors, we consider low-level airflow characteristics (the 925- and 850-hPa direction and along-valley wind speed) and low-level stability (0–2500-m mean moist Brunt–Väisälä frequency N_m^2) in Fig. 5.

Starting with low-level moist static stability, deep[4] down-valley flow was generally characterized by stable conditions ($N_m^2 > 0\,\mathrm{s}^{-2}$). Shallow reversed flow did not correspond to any particular stability condition, with both weakly stable and unstable conditions noted during shallow events. The strong correlation ($r = 0.61$) between N_m^2 and down-valley flow depth indicates that flow blocking/deflection is likely contributing to the deepest flow-reversal events in the Quinault

[4] For the remainder of this section (section 3a), references to "deep down-valley flow" include both categories of deep down-valley flow, i.e., those that extended offshore and those that did not extend offshore.

Brought to you by University of Washington Libraries | Unauthenticated | Downloaded 08/28/24 11:35 PM UTC

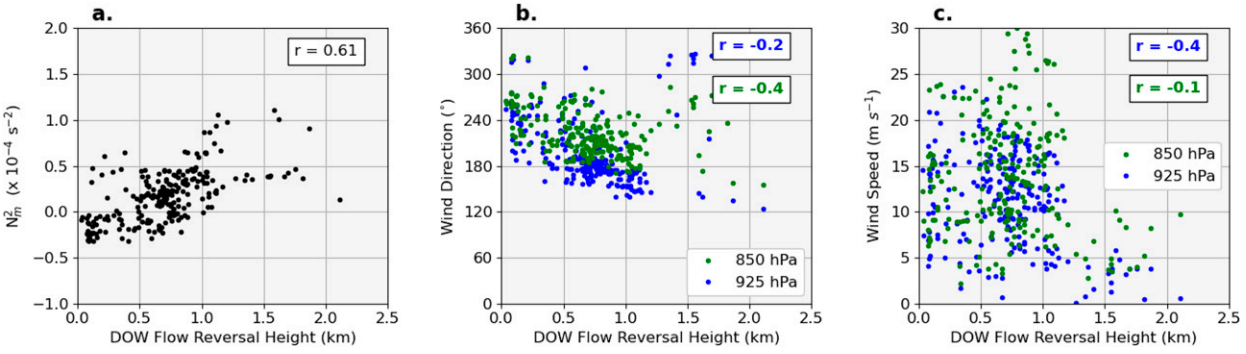

FIG. 5. Scatterplots showing the relationships between the down-valley flow depth over the DOW compared to (a) moist static stability (N_m^2), (b) wind direction, and (c) wind speed. The plots in (b) and (c) are further delineated by level, with green icons indicating the 850-hPa wind characteristics and blue icons indicating the 925-hPa wind characteristics. Correlation coefficients are shown in each panel. Each icon represents 1 h of observed down-valley airflow.

Valley, consistent with other studies which described environmental conditions during down-valley flow (e.g., Whiteman and Doran 1993; Carbone et al. 1995; Steiner et al. 2003; Rotunno and Houze 2007).

Wind direction at 850 hPa (925 hPa) was increasingly southerly (southeasterly) as down-valley flow depth increased. Over the region, several studies have associated these veering wind profiles with the prefrontal sectors of midlatitude cyclones approaching the valley, with a robust signal of stable or near-neutral moist static stability within those storm sectors (McMurdie et al. 2018; Zagrodnik et al. 2019, 2021). This suggests that down-valley flow in the region is more common during the prefrontal sector of landfalling midlatitude cyclones, consistent with the studies of Colle and Mass (1996) over western Washington and of Asencio and Stein (2006) in the Italian Alps.

Upstream wind speed at 850 hPa showed no substantial relationship with down-valley flow depth—likely because wind at 850 hPa is well above the height of most terrain in the vicinity of the Quinault Valley. Lower in the atmosphere, at 925 hPa, there was a modest negative relationship between wind speed and down-valley flow height, especially for deep flow reversals. Conceptually, this aligns with earlier discussions of flow blocking, as the deeper down-valley flows tend to be more blocked, which requires weaker winds that cannot surmount the barrier.

To summarize the above discussion, deep down-valley flow within the Quinault Valley was associated with stable conditions in the presence of southerly low-level winds, a strong positive SEA–HQM pressure difference, and large values of the nondimensional mountain height. This combination of metrics indicates that deep down-valley flows were likely due to flow blocking and the resultant deflection of airflow around the Olympic Mountains. However, during cases of shallower down-valley flow these relationships become substantially less clear and flow blocking becomes a less likely explanation. For shallower cases, the SEA–HQM pressure difference and upstream stability were often negative (onshore and unstable, respectively) and there was a wide range of wind speeds and directions. Such variability of these metrics underscores the complex nature of down-valley flow in the Quinault Valley and points to other causes of low-level flow reversals, such as drainage flows, mechanical reversals, mesoscale pressure considerations, or negative buoyancy resulting from latent heat absorption.

b. *Forecasts of down-valley flow during OLYMPEX*

Next, we consider whether or not numerical weather prediction models were able to forecast reversed flow in the Quinault Valley during OLYMPEX and whether simulated reversed flow occurred within the same environmental conditions as were observed. To investigate this, 6-hourly archived forecasts (1.33-km horizontal resolution) from the OLYMPEX campaign were used, resulting in 32 model–observation pairs. Consistent with the radar processing described previously, the height of down-valley flow in the model was determined by considering the simulated radial wind 5–15 km up-valley from the DOW along the 58.4° azimuth. Simulated upstream environmental conditions (e.g., sea level pressure differences, N_m^2, and wind characteristics were calculated at the NPOL radar in the same manner as the NARR data described previously. These simulations used the Advanced Research version of the Weather Research and Forecasting (WRF-ARW, hereafter referred to as WRF) Model (Skamarock et al. 2008) version 3.7.1, in a configuration used by the University of Washington (UW) in its real-time operational weather forecasts.[5] Additional model configuration information about the UW WRF can be found in Conrick and Mass (2019). For this section, we considered short-range forecasts initialized daily at 0000 UTC, with lead times ranging from 6 to 24 h. An evaluation of forecast synoptic accuracy can be found in appendix B.

At 1.33-km horizontal resolution, simulations reproduced most of the observed environmental conditions that supported down-valley flow in the Quinault Valley. As with the observations outlined above, the simulated SEA–HQM pressure difference and the simulated nondimensional mountain height were noted as being well-correlated with the reversed flow depth (Figs. 6a,b). Also consistent with observations, stable

[5] See the University of Washington WRF page for more information: https://a.atmos.washington.edu/wrfrt/.

Brought to you by University of Washington Libraries | Unauthenticated | Downloaded 08/28/24 11:35 PM UTC

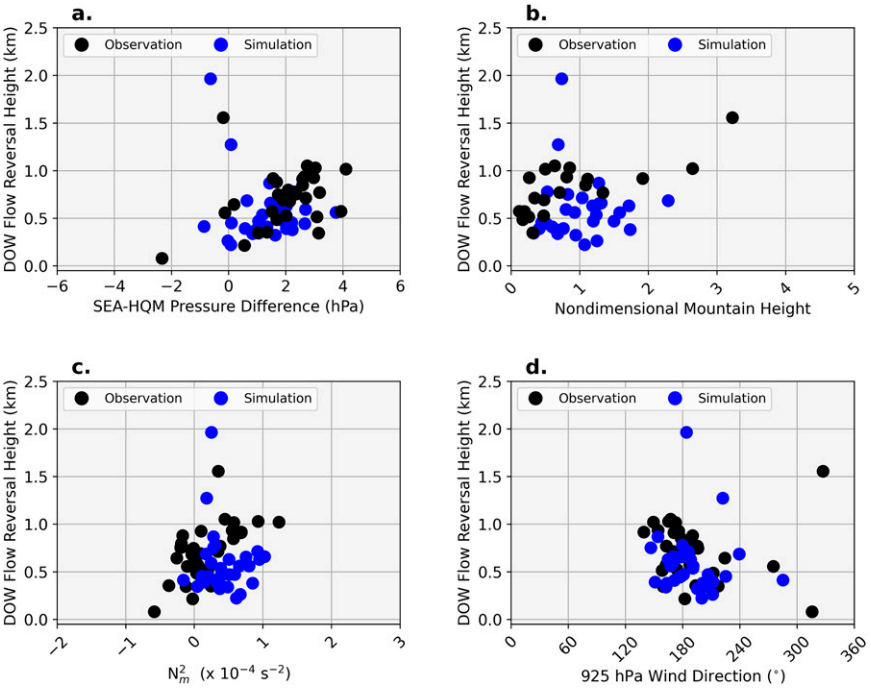

FIG. 6. Relationships between down-valley flow depth and environmental conditions based on observations and simulations: (a) SEA–HQM pressure difference, (b) nondimensional mountain height, (c) 0–2500-m mean moist static stability, and (d) 925 hPa wind direction. Each icon represents 1 h of down-valley airflow.

simulated conditions and southerly 925-hPa wind direction coincided with down-valley flow periods (Figs. 6c,d).

There were, however, a few notable differences between the observed and simulated environments. The WRF forecasts tended to be more stable (mean $N_m^2 = 0.41 \times 10^{-4}\,s^{-2}$) compared to observations (mean $N_m^2 = 0.18 \times 10^{-4}\,s^{-2}$), though that was likely from using the much coarser NARR as observations, which may not adequately resolve local terrain. The mean simulated SEA–HQM pressure difference (1.21 hPa) was also weaker than observed (1.95 hPa), which may have contributed to somewhat shallower down-valley flow in the forecasts, with a mean model–observation difference of −52 m. Shallower-than-observed simulated down-valley flow was also noted by Thériault et al. (2012) in wintertime simulations near Vancouver, Canada. Differences in the speed of synoptic-scale features (e.g., cold or warm frontal passage) compared with observed times may also contribute to differences between simulated and observed flow. Nevertheless, the operational WRF-ARW model used during OLYMPEX was able to capture the key elements of down-valley flow events.

c. *Precipitation patterns during observed down-valley flow*

The impact of down-valley flow on local precipitation patterns remains an outstanding question (Rotunno and Houze 2007), especially outside of individual case studies (e.g., Bousquet and Smull 2003). In this section, we consider precipitation from 20 rain gauge sites throughout the Quinault Valley and surrounding areas during periods of down-valley flow.

Figure 2b shows the mean rain rate at the 20 rain gauge sites around the region during all 285 h of data. Mean rain rates increased from the coast to the middle of the valley (the approximate location of the DOW radar), then decreased as elevation increases toward the northeast. The higher-elevation windward ridges saw the greatest average rain rates during the campaign as also noted by Houze et al. (2017). This pattern of precipitation enhancement has also been noted in other OLYMPEX studies (i.e., Houze et al. 2017; Purnell and Kirschbaum 2018; Zagrodnik et al. 2018, 2019, 2021; Conrick and Mass 2019).

Precipitation patterns were altered when down-valley flow was present. Figure 7 shows the departure from the mean precipitation rate for each class of down-valley flow. When deep reversed flow extended offshore, precipitation enhancement relative to the mean was confined to a narrow region immediately along the coast, rather than farther inland when the reversed flow did not extend offshore (cf. Figs. 7a,b). Precipitation during shallow down-valley flow tended to be less than the mean across most of the region (Fig. 7c), similar to the precipitation patterns noted by Zagrodnik et al. (2019) during prefrontal storm sector environments. Broadly speaking, down-valley flow reduced precipitation rates in the Quinault Valley.

A noteworthy aspect of the precipitation patterns presented in Fig. 7 is the transition from positive to negative departures from the mean near the coast when deep down-

Brought to you by University of Washington Libraries | Unauthenticated | Downloaded 08/28/24 11:35 PM UTC

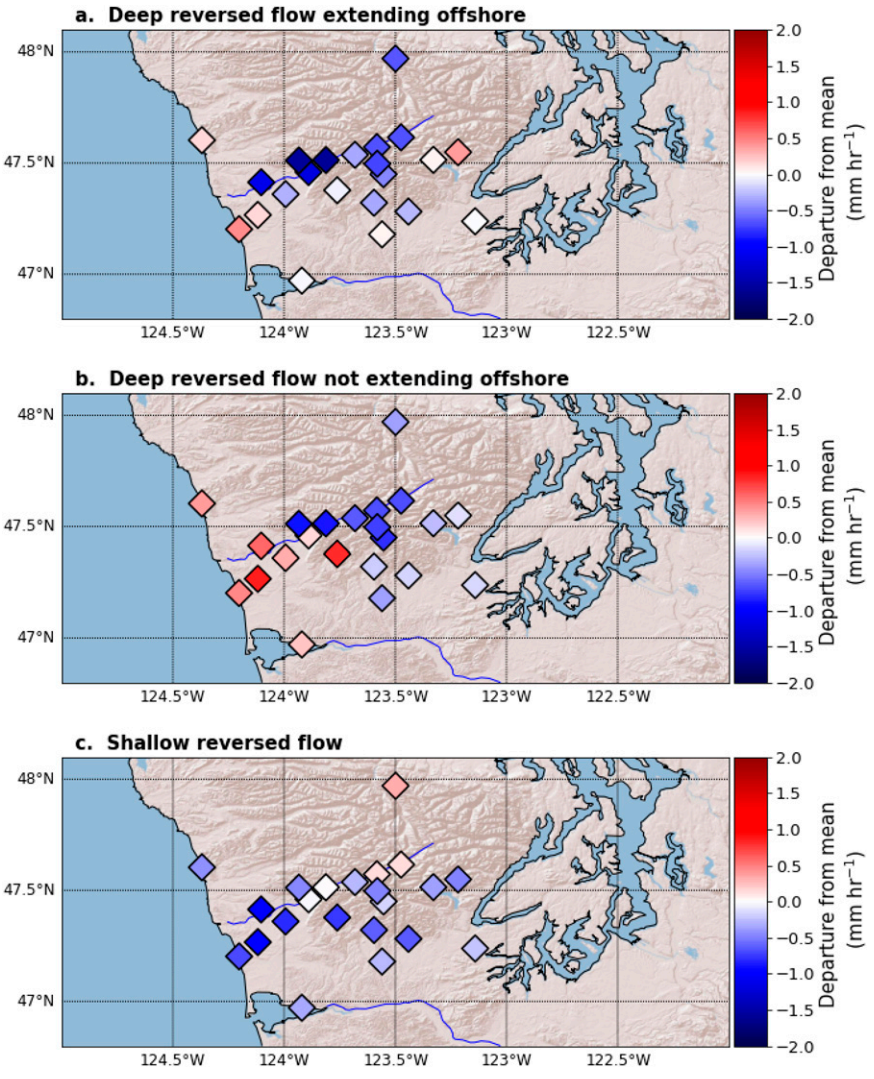

FIG. 7. Maps depicting the departure of precipitation rate from the mean of the 285 h of observations. Departures are separated by (a) deep reversed flow that extended offshore, (b) deep reversed flow not extending offshore, and (c) shallow reversed flow.

valley flow was present. With stable conditions at low levels in place during deep down-valley flow, it is reasonable to hypothesize that the transition from positive to negative precipitation anomalies is due to the spatial extent and strength of the stable air near the surface. Similar patterns have been noted in other studies, most notably Houze et al. (2001), James and Houze (2005), and Zagrodnik et al. (2019), which showed precipitation enhancement upstream of topography when flow is lifted over stably stratified lower levels of the atmosphere.

4. Case study: 16–17 November 2015

This section considers a case study of down-valley flow during the OLYMPEX campaign. The case study chosen is the down-valley flow event of 16–17 November 2015, which exhibited a prolonged period of deep reversed flow in the Quinault Valley followed by a transition to up-valley flow. High-resolution model simulations and observations from the event are used to understand how cooling from evaporation and melting may have affected the down-valley flow that was observed during the event.

a. Model configuration

Model simulations in this section used version 4.1.3 of the WRF Model. The model domain configuration consisted of nested domains (Fig. 8) each with 51 vertical levels that were distributed according to the hybrid vertical coordinate option available in WRF (Klemp 2011). The innermost 1.33-km domain was centered over the Olympic Peninsula. A 48-h simulation was completed, with initialization at 0000 UTC 16 November 2015. Initial and boundary conditions were

Brought to you by University of Washington Libraries | Unauthenticated | Downloaded 08/28/24 11:35 PM UTC

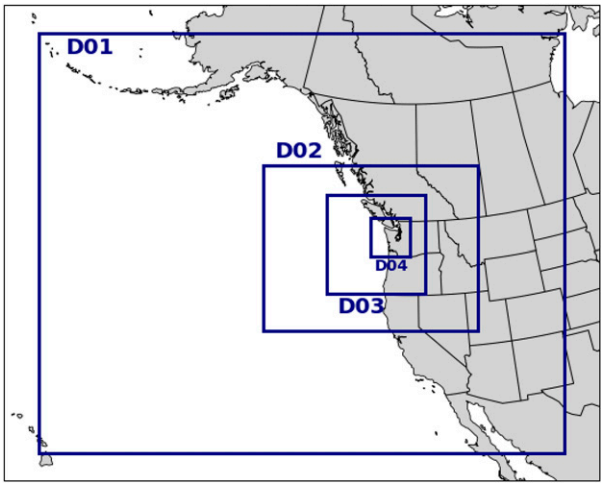

FIG. 8. Map of the nested WRF Model domains used in this study.

obtained from the 0.25° Global Forecast System (GFS) gridded analysis dataset. The boundaries of the outermost (36 km) domain were updated every 3 h using either the GFS initialization (0000, 0600, 1200, and 1800 UTC) or the 3-h GFS forecast (0300, 0900, 1500, and 2100 UTC). The outermost domain was also nudged every 3 h toward the GFS conditions.

To simulate microphysical processes, the Thompson–Eidhammer aerosol-aware microphysics option (Thompson and Eidhammer 2014) was used. Additional information about model parameterization selections can be found in Table 1. Furthermore, the cumulus scheme (Grell–Freitas; Grell and Freitas 2014) was not used on the innermost (1.33-km) domain. The accuracy of this simulation, compared to NARR, is described in appendix B.

b. *Meteorological overview*

The 16–17 November 2015 event was part of an active period during OLYMPEX. The event was characterized by the approach of a broad upper-level trough over the Gulf of Alaska, with a modest low (1200-m geopotential height) at 850 hPa (Fig. 9a) and a 982-hPa surface low offshore of British Columbia at 1200 UTC 16 November. South of the low center, an expansive warm, moist airmass extended westward over the North Pacific (Figs. 9b,c). This plume of moisture was advected

TABLE 1. WRF-ARW parameterization choices used in this study.

Parameterization type	Chosen configuration	Reference
Microphysics	Thompson–Eidhammer	Thompson and Eidhammer (2014)
Land surface	Noah-MP	Niu et al. (2011)
Radiative transfer	RRTMG	Iacono et al. (2008)
Cumulus	Grell–Freitas	Grell and Freitas (2014)
Boundary layer	Yonsei University (YSU)	Hong et al. (2006)

by ~40 kt (~20.5 m s^{-1}) 850-hPa west-southwesterly winds, impacting the Quinault Valley between 0000 and 2000 UTC 17 November and producing more than 100 mm of precipitation over the region during that time (Conrick and Mass 2019).

The early stage of the 16–17 November event was characterized by a prolonged, offshore-directed pressure gradient across the region, which resulted from the approaching surface low and its associated warm front that was just offshore of the Olympic Peninsula at 1200 UTC 16 November (Figs. 9, 10a–c). Figures 10a–c shows an overview of the regional surface pressure fields 6 h before (Fig. 10a) and after (Fig. 10c) the event's period of peak down-valley flow, which is shown in Fig. 10b. The SEA–HQM pressure difference was positive (offshore) 6 h prior and during peak down-valley flow, then negative 6 h after the peak. The observed pressure difference corresponded to a 90th percentile event among the 228 h of down-valley flow considered in section 3.

Regional low-level moist static stability was also characteristic of down-valley flow, with initially neutral stability transitioning to stable conditions as the event's warm front interacted with the coastline (Figs. 10d–f). The largest values of N_m^2 coincided with the greatest SEA–HQM pressure differences, indicative of blocked airflow.

Following warm frontal passage, weakening of the SEA–HQM pressure difference and the decrease in low-level stability after 0000 UTC coincided with a gradual erosion of the low-level flow reversal near the DOW (Fig. 11a). The offshore pressure gradient peaked at 0030 UTC (3.17 hPa), then steadily weakened until becoming negative (onshore) after 0500 UTC. Approximately 2 h later, the down-valley flow

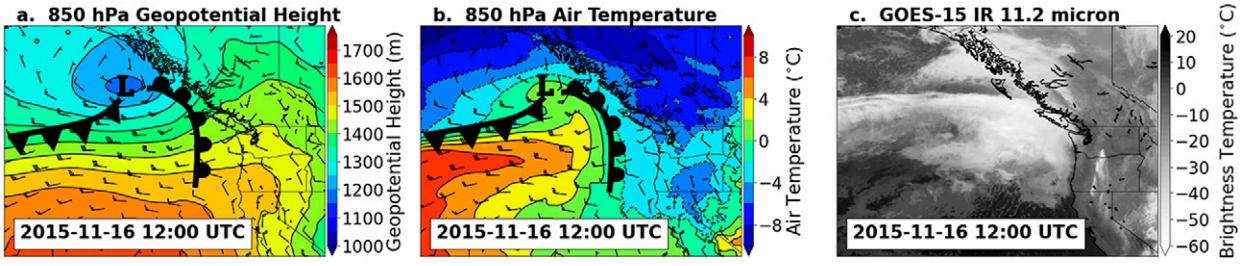

FIG. 9. Maps of the representative synoptic situation at 1200 UTC 16 Nov 2015, including (a) 850-hPa geopotential height, (b) 850-hPa air temperature, and (c) *GOES-15* infrared brightness temperature. Data in (a) and (b) come from the NARR dataset. The surface low and corresponding surface frontal boundaries are plotted in (a) and (b), following common conventions.

Brought to you by University of Washington Libraries | Unauthenticated | Downloaded 08/28/24 11:35 PM UTC

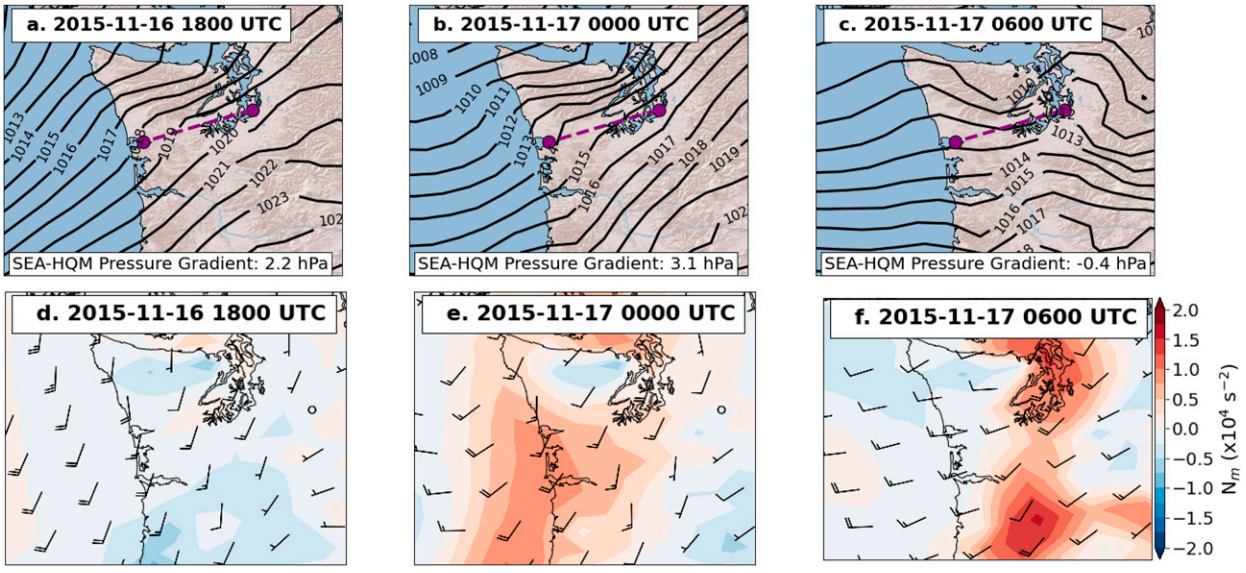

FIG. 10. (a)–(c) Sea level pressure (SLP) contoured every 1 hPa at 6-h intervals and (d)–(f) 6-h 950–850-hPa mean moist static stability (N_m^2) and the mean 925–850-hPa wind from NARR data. In (a)–(c), the pressure observation locations of Seattle, WA (SEA), and Hoquiam, WA (HQM), are shown, along with a dashed line connecting them to represent the region over which the SEA–HQM pressure difference was computed. All data come from NARR data.

layer began responding to the weaker pressure gradient, with a steady decrease in depth from 0230 UTC until the layer became difficult to detect after 1000 UTC. It is important to note that the time series in Fig. 13a begins with down-valley flow because precipitation was not detected by the radar prior to ~1400 UTC.

Precipitation patterns during the event approximately followed the patterns outlined in Fig. 7. When down-valley flow was deep and extended ~15 km offshore (2300 UTC 16 November; see Fig. 3a), precipitation was light at all sites shown except at the Seed Orchard, which is nearest the coast (Fig. 11b). The spike in precipitation appeared to be at least partially caused by air lifting over the sharp leading edge of the cooler, denser airmass associated with the combination of down-valley flow within the Quinault valley and regional-scale blocking extending to the coast. As the lower layer retreated and became somewhat shallower (~0300 UTC 17 November; Fig. 3b), precipitation at all stations was modestly elevated (5–10 mm h^{-1}), consistent with the pattern shown in Fig. 8b. As the reversed flow became shallower, there was a noted

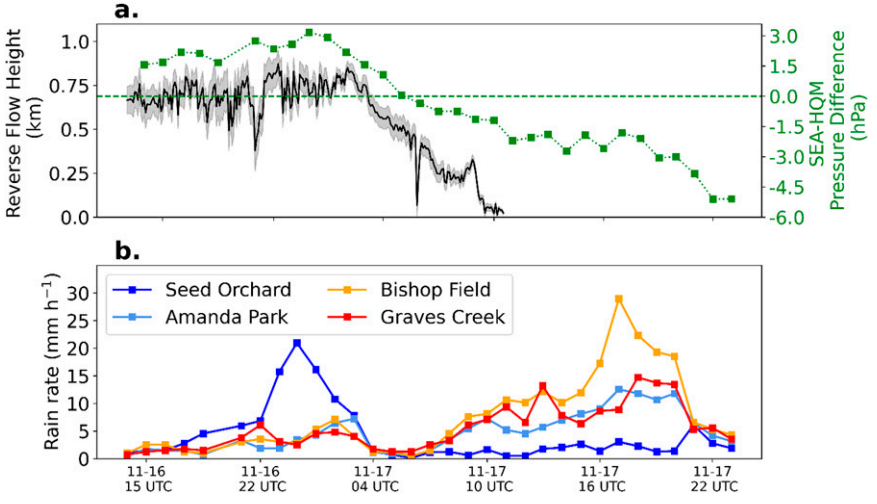

FIG. 11. (a) Time series of the down-valley flow depth from (left) the DOW (km) and (right) the SEA–HQM pressure difference (hPa) over the period from 1200 UTC 16 Nov to 0000 UTC 18 Nov. The black solid line indicates the mean depth of the down-valley flow layer, with the gray region indicating $\pm 1\sigma$ (standard deviation). (b) Time series of rain rates at select Quinault Valley locations corresponding to the lettered observing sites in Fig. 2b. (S: Seed Orchard; A: Amanda Park; B: Bishop Field; and G: Graves Creek).

Brought to you by University of Washington Libraries | Unauthenticated | Downloaded 08/28/24 11:35 PM UTC

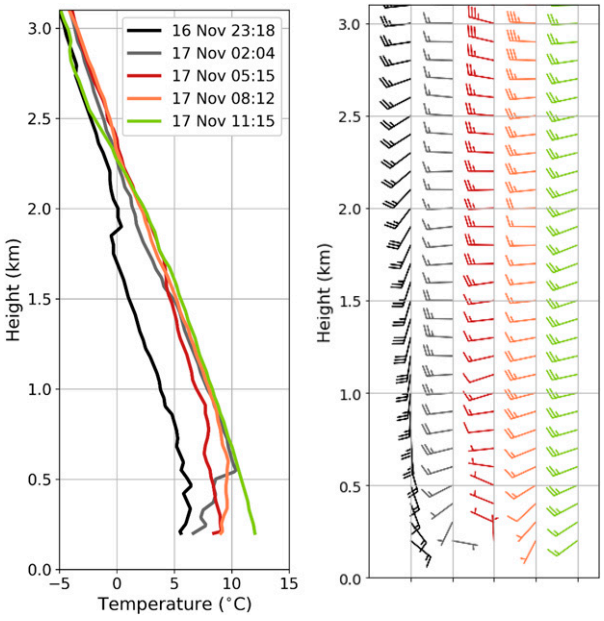

FIG. 12. Vertical profiles of (left) temperature (°C) and (right) wind speed and direction taken from soundings launched at the NPOL radar site near the location where the Quinault River meets the Pacific Ocean. Altitude is relative to sea level. Colors in the right panel correspond to the legend in the left panel. The half barbs represent wind 1–10 m s^{-1}.

decrease in precipitation at all sites from 0400 to 0700 UTC (Fig. 11b; example shown in Fig. 3c). After 0700 UTC, as the down-valley flow was dissipating, rain rates at all stations increased in intensity, with the largest rain rates at the Bishop Field site in accordance with the transition to unblocked flow in the midlatitude cyclone's warm sector.

Figure 12 uses soundings launched at ~3-h intervals from the NPOL radar site to connect the event's low-level stability with the event's descending warm frontal inversion. The warm front passage was evident from the jump in temperature between 2318 UTC 16 November and 0204 UTC 17 November. However, colder air remained in place near the surface for 8–10 additional hours after the warm front passage. At 0204 UTC 17 November, the colder layer was ~0.5 km deep and was capped by the frontal inversion. From 0515 to 0812 UTC, the frontal inversion continued to descend and was located close to the surface ~0.25 km above sea level (~0.1 km above ground level). Finally, by 1115 UTC 17 November, the colder stable layer was not detected by the sounding, although it still may have been present below the elevation of the sounding site (150 m). Wind profiles, also shown in Fig. 12, show that the descending warm frontal inversion corresponded with a shift from offshore wind to onshore flow. This progression is consistent with low-level flow blocking eroding with the approach of the cyclone's warm front.

With both blocked airflow and the regional pressure gradient as contributors to down-valley airflow during the event, it is important to point out that these two factors acted together. Initially, an offshore-directed pressure gradient was responsible for forcing air down the Quinault Valley. At later times, the approach of the system's warm front contributed to stable low levels of the atmosphere near the Pacific Coast, which promoted flow blocking and sustained down-valley flow within the Quinault Valley. This conclusion can be drawn by considering the presence of down-valley airflow in relation to the local pressure difference (Fig. 11a) and low-level stability (Fig. 10).

c. *Simulated down-valley flow*

In our simulation of the 16–17 November 2015 event, the Control simulation produced down-valley flow during the approximate times that it was observed by the DOW radar

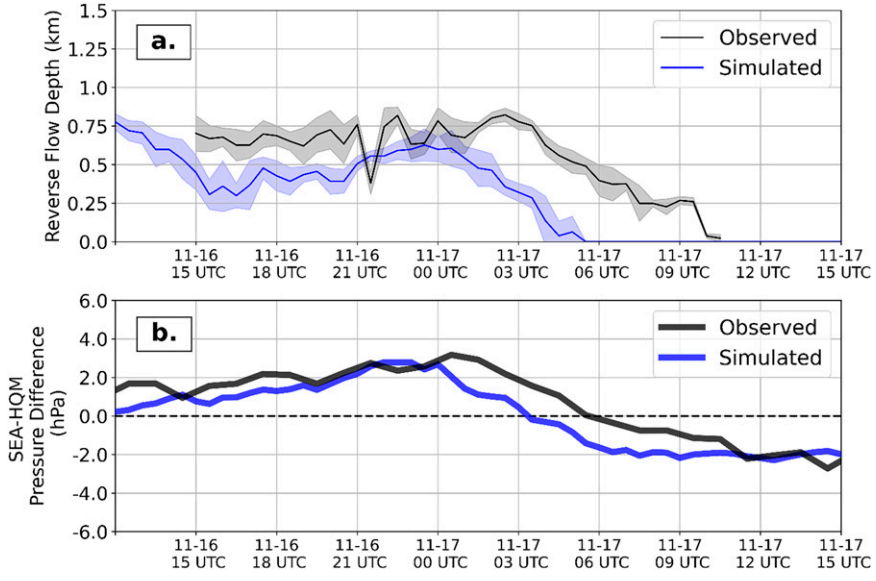

FIG. 13. Time series of 30-min mean (a) simulated (blue) and observed (black) down-valley flow depth (km), where the solid line is the mean value and $\pm 1\sigma$ is shown in the shaded region, and (b) the simulated (blue) and observed (black) SEA–HQM pressure difference.

Brought to you by University of Washington Libraries | Unauthenticated | Downloaded 08/28/24 11:35 PM UTC

(Fig. 13). Notably, the model realistically simulated the timing of the most significant down-valley flow (1500 UTC 16 November–0100 UTC 17 November). However, during that period, the depth of the simulated reversed flow averaged 253 ± 103 m shallower than observations (Fig. 13a), a situation which may be the result of overzealous boundary layer mixing during stable conditions by the YSU scheme (Wilson and Fovell 2018), though tests conducted with the MYNN (Nakanishi and Niino 2006) boundary layer scheme did not yield significantly different results (not shown). Simulated down-valley flow that is shallower than observed was also noted by Thériault et al. (2012) in wintertime simulations near Vancouver, Canada.

Starting at 0100 UTC 17 November, down-valley flow in the Control began to erode, which was ~2 h sooner than observed by the DOW. Moreover, after 0500 UTC almost no down-valley flow was present in the simulation, whereas the DOW detected weakening down-valley flow conditions for several more hours until 1000 UTC. The earlier decline of the simulated SEA–HQM pressure difference, shown in Fig. 15b, is considered the reason for the earlier erosion of simulated down-valley flow and appears to result from an earlier warm frontal passage than was observed. The observed positive (offshore) pressure difference peaked around 0000 UTC, then gradually declined until becoming negative at 0500 UTC. In contrast, the simulated pressure difference peaked around 2200 UTC and became negative around 0300 UTC. Nevertheless, the model was able to capture the event's down-valley flow and associated pressure characteristics.

d. *Effects of latent heating*

With dynamics and the regional pressure gradient as the primary driver of down-valley flow prior to ~1800 UTC 16 November, we turn our attention to the period after 1800 UTC 16 November to understand how the evaporation and melting of hydrometeors may have affected the event. Two additional numerical simulations were conducted, both of which were identical in configuration to the simulation described in section 4a (hereafter the Control). The first experiment, called "NoEvap," removes the temperature tendency resulting from the evaporation of rainwater (i.e., rain falling into a subsaturated environment). The second, called "NoMelt," removes the cooling effects of melting snow and graupel hydrometeors from the simulation. In both simulations, only the temperature tendency is impacted, with the microphysical processes allowed to function as otherwise intended.

First, we consider the temperature tendencies from the microphysics parameterization in the Control simulation to determine when each microphysical process was active in the vicinity of the DOW radar (Fig. 14). The total microphysical temperature tendency was broadly characterized by condensational heating aloft and strong cooling at and below the level of the flow reversal. Considering evaporation, Fig. 14b, the cooling tendency did not extend outside of the down-valley flow layer, with its maximum magnitude occurring around 0000 UTC 17 November. Melting of hydrometeors resulted in a cooling tendency concentrated just below the melting level (0°C level) from 1800 UTC 16 November and after,

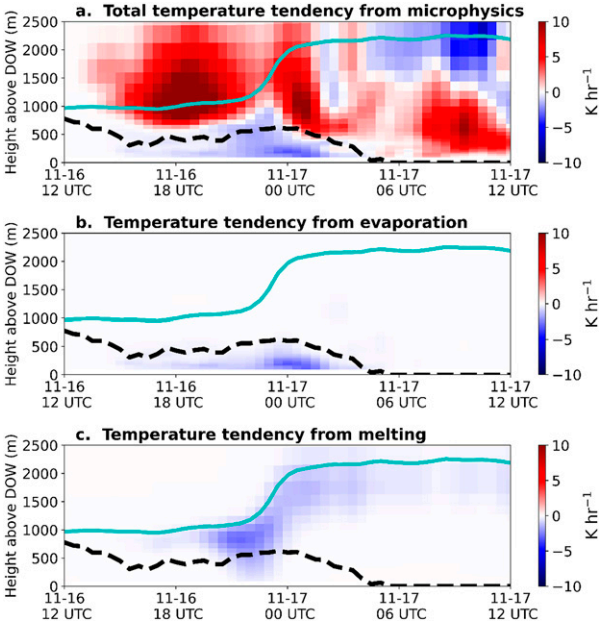

FIG. 14. Time–height cross sections over the DOW radar of microphysical temperature tendency from the Control simulation. Red colors indicate warming and blue colors indicate cooling. (a) The total temperature tendency, (b) the temperature tendency from evaporation of rain, and (c) the temperature tendency from melting snow and graupel. The black dashed line is the simulated depth of down-valley flow and the cyan line shows the melting-level height.

though just before the passage of the warm front (2100 UTC 16 November), cooling due to melting extended to the surface for a brief (~2 h) period (Fig. 14c).

Figure 15 shows time series of the down-valley flow depth over the DOW from the Control, NoEvap, and NoMelt experiments. Before 1500 UTC 16 November, there was little to no difference between simulations. As precipitation began to affect the region after 1500 UTC, the three simulations began to diverge. Without melting influencing temperatures, the down-valley flow depth in the NoMelt simulation was modestly (~100 m) shallower than the Control from 1900 to 2200 UTC, corresponding to the period when air temperatures over the DOW and within the flow reversal layer were most affected by melting (Fig. 14c). After 2200 UTC, the melting level rose rapidly as the warm sector arrived, which reduced the impact of melting-induced temperature change within the flow reversal layer.

Down-valley flow was more affected by the NoEvap than the NoMelt experiment. Evaporative cooling, while present throughout the period of precipitation, had its greatest magnitude between 2200 and 0200 UTC after the passage of the warm front, which is around the time when down-valley flow in the NoEvap experiment began to decrease in depth. By 0300 UTC 17 November, the flow reversal had ended in the NoEvap experiment, contrasting with the Control and NoMelt, which retained down-valley flow for another 3 h until 0600 UTC.

The conclusion that can be drawn is that evaporation, rather than melting, had a greater impact on the 16–17 November event. It appears that because evaporative cooling was

Brought to you by University of Washington Libraries | Unauthenticated | Downloaded 08/28/24 11:35 PM UTC

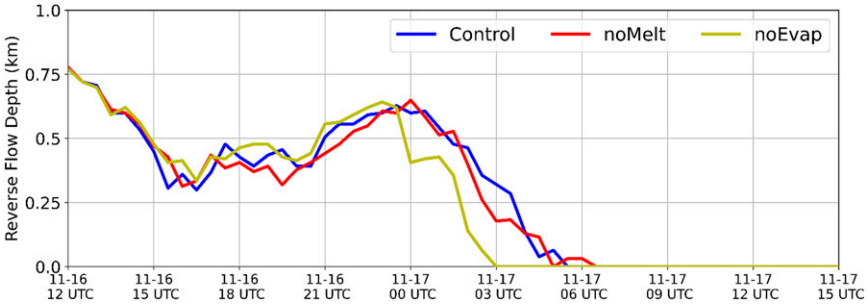

FIG. 15. Time series of 30-min mean simulated down-valley flow depth (km) from the Control (blue), NoMelt (red), and NoEvap (yellow) simulations.

exclusively confined to the near-surface down-valley flow layer, it had a greater role in maintaining down-valley flow during the event than melting did. On the other hand, melting generally only cooled the atmosphere directly above the down-valley flow layer except for a brief ~2-h period during the warm frontal passage. We conclude that this particular event would have been shorter in duration if no evaporative cooling were present, but the deep down-valley flow would have occurred nonetheless.

Next, we consider three times during the event, 1200 UTC 16 November, 2100 UTC 16 November, and 0100 UTC 17 November to elucidate how factors impacting down-valley flow (e.g., stability, air temperature, and sea level pressure) were affected by our latent heating experiments. These three times were chosen based on Figs. 14 and 15 as the periods when there was no difference in down-valley flow depths among simulations, when melting-induced cooling was strongest below the height of down-valley flow, and when evaporative cooling was most significant below the flow reversal, respectively.

The spatial and temporal evolution of simulated 0–1-km mean moist static stability (N_m^2) and 10-m and 1-km wind is shown in Fig. 16 and offers insight into how evaporation and melting influenced the lower atmospheric environment. A value of 1 km was chosen as the ceiling for these metrics because the simulated flow reversal does not extend more than 1 km above ground.

Consistent with the down-valley flow depths shown in Fig. 15, only minor differences in simulated wind and stability characteristics were noted at 1200 UTC 16 November. Nine hours later, at 2100 UTC, low-level stability in the Quinault Valley in the NoMelt simulation had slightly increased as a result of elevated warming, though stability was generally most similar to the Control. In the NoEvap simulation, the lower atmosphere was much less stable than the Control in the Quinault Valley due to a lack of evaporative cooling affecting low-level air temperatures. Wind characteristics among simulations showed only minor differences at that time. At 0100 UTC 17 November, low-level stability in the NoMelt simulation was similar to the Control, but NoEvap showed less stable conditions due to the lack of evaporative cooling, mostly in the windward valleys (such as the Quinault Valley) and along the Pacific coast. While wind is qualitatively similar between the Control and NoMelt, the down-valley wind between DOW and NPOL in NoEvap is less directionally coherent than the Control, confirming the role of evaporative cooling in prolonging the down-valley flow past 0000 UTC. These three times highlight the more substantial influence of evaporation, rather than melting, on low-level stability due to evaporation occurring exclusively within the low-level down-valley flow layer.

An interesting aspect of Fig. 16 is the difference between the 10-m and 1-km winds at 0100 UTC 17 November in all three simulations. The wind shift associated with the approaching warm front is noted as extending from northwest to southeast. In the system's warm sector (i.e., west of the wind shift), the wind direction at each level is approximately the same. In contrast, the 10-m wind direction in the prefrontal sector is east or northeast, contrasting with the westerly winds at 1 km. Such vertical directional wind shear is consistent with the low-level flow being blocked. Moreover, it appears that the warm frontal wind shift occurred earlier when evaporative cooling was turned off in the NoEvap simulation.

Finally, the faster warm front along the coast in NoEvap can be explained by considering temperature and pressure differences at the time when down-valley flow was dissipating in the NoEvap simulation (0100 UTC 17 November). Figures 17a and 17d show the 0–1-km average evaporation and melting rates, respectively, from the Control simulation, highlighting that low-level evaporation was much more pronounced than melting within the windward valleys of the Olympic Mountains, as was shown in Fig. 14. As a consequence, without evaporative cooling, air temperatures were as much as 2°–4°C warmer than the Control along the Washington coast and windward areas of the Olympic Mountains, especially windward valleys. This resulted in lower (1–2.5 hPa) sea level pressure in the NoEvap simulation compared to the Control over a region that already had locally higher pressure, resulting in a faster forward frontal motion. In contrast, the NoMelt simulation showed less warming and a less pronounced pressure difference than NoEvap.

Synthesizing the above analyses, it appears that evaporation, rather than melting, played an important role in prolonging the down-valley flow event of 16–17 November down-valley airflow event. We hypothesize that because evaporation occurred over a more extended period compared to melting *and* because evaporation was confined to the layer of the

Brought to you by University of Washington Libraries | Unauthenticated | Downloaded 08/28/24 11:35 PM UTC

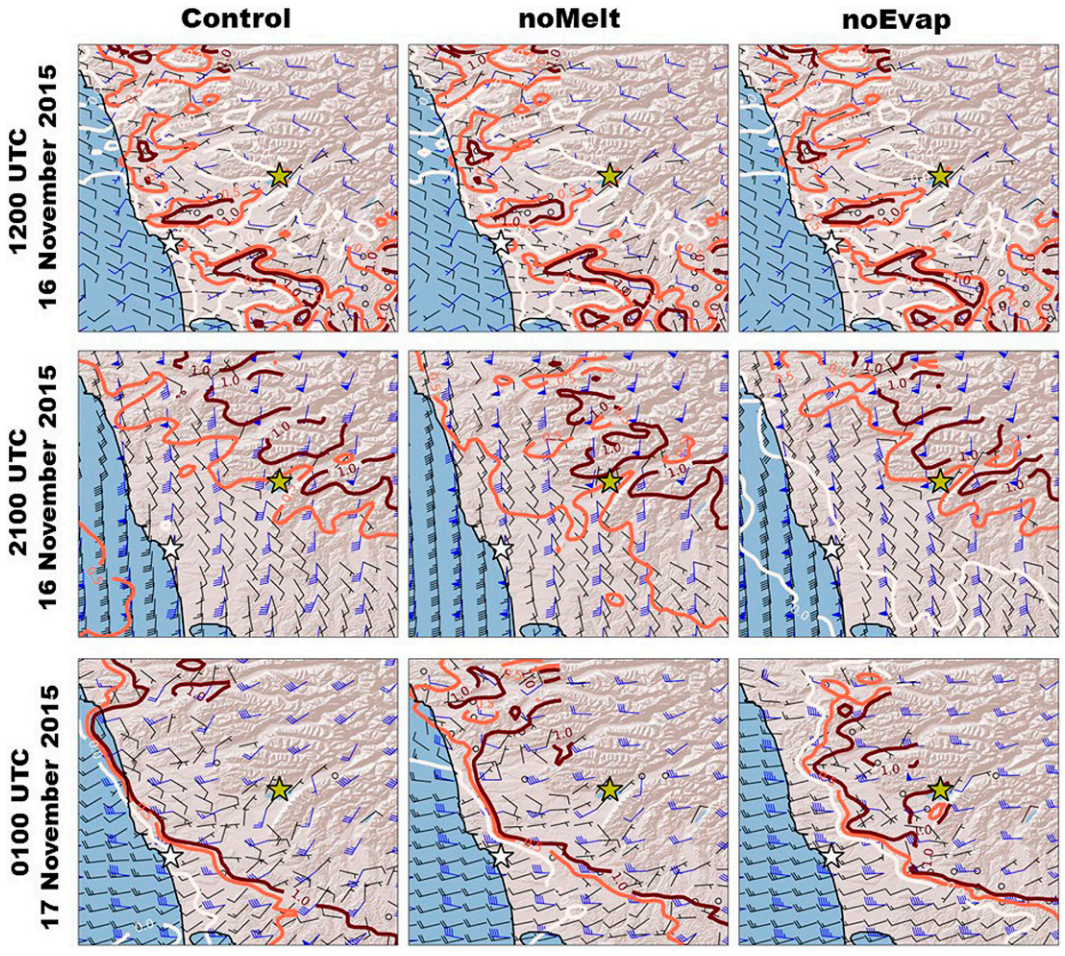

FIG. 16. Simulated 0–1-km moist static stability (N_m^2; colored contours; white: 0×10^{-4} s^{-2}; green: 0.5×10^{-4} s^{-2}; black: 1×10^{-4} s^{-2},), 10-m wind (black barbs), and 1-km wind (blue barbs) at (top) 1200 UTC 16 Nov, (middle) 2100 UTC 16 Nov, and (bottom) 0100 UTC 17 Nov for each simulation (columns). Wind barbs are altered from the typical convention as follows: a half barb is 2.5 m s^{-1}, a full barb is 5 m s^{-1}, and a flag is 25 m s^{-1}. The yellow (white) star shows the DOW (NPOL) location.

atmosphere within the flow reversal, it was more effective at cooling the lower levels of the atmosphere. Such cooling not only ensured that air remained stable for longer but also maintained higher pressure on the windward side of the Olympics during the event, which slowed the progression of the warm front and its associated wind shift. Moreover, the effects of evaporation can be considered as part of a feedback mechanism: Drier synoptically driven down-valley flow promoted evaporation, increased lower atmospheric stability, and allowed down-valley flow to persist for several hours after the passage of the warm front. Warm frontal passage ultimately was responsible for shifting the airflow in the vicinity of the valley to up-valley flow.

5. Discussion and conclusions

This study investigated the characteristics of down-valley flow within the Quinault Valley of Washington State. During the OLYMPEX field experiment, the Quinault Valley was heavily instrumented to provide extensive observations of precipitation and microphysics during midlatitude cyclones as they impacted the Olympic Peninsula. Radar observations collected from the DOW and NPOL radars during the period from November 2015 to January 2016 provided a sample of 285 h of precipitation. Down-valley flow was the dominant regime, occurring in 228 of the 285 h (80%). The hours of reversed airflow were separated into three categories: 1) deep (>500 m) down-valley flow that extended offshore, 2) deep down-valley flow that did not extend offshore, and 3) shallow (<500 m) down-valley flow.

Using upstream NARR and information obtained from radar RHI scans, we described the conditions during which down-valley flow occurred. Two key metrics were used: 1) the pressure difference between Seattle, WA (SEA) and Hoquiam, WA (HQM; on the Washington coast) and 2) the nondimensional mountain height. The SEA–HQM pressure difference served as a metric of the large-scale near-surface airflow along the long axis of the valley. The nondimensional mountain height

Brought to you by University of Washington Libraries | Unauthenticated | Downloaded 08/28/24 11:35 PM UTC

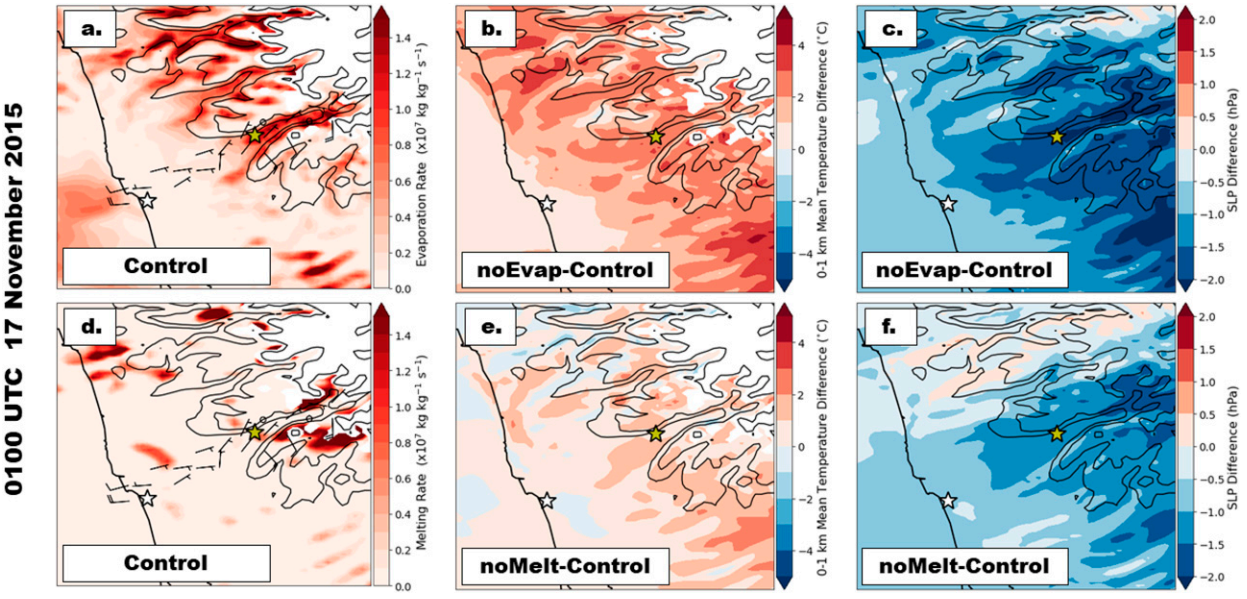

FIG. 17. (a),(d) Simulated evaporation and melting process rates, respectively. (b),(c) The NoEvap minus Control differences of 0–1-km mean air temperature and sea level pressure, respectively. (e),(f) As in (b) and (c), but for the noMelt minus Control differences. All panels are valid at 0100 UTC 17 Nov 2015.

is a widely used metric quantifying the presence and strength of flow blocking. Both were shown to be correlated with the depth of down-valley flow in the Quinault Valley. In particular, we demonstrated that deep down-valley flow occurred in environments where the upstream environment was blocked and the SEA–HQM pressure difference was large and positive (offshore-directed). Shallow events were not associated with a particular pressure or blocking configuration.

Analysis of upstream airflow characteristics (moist static stability N_m^2 and 925- and 850-hPa wind) showed that there was a strong positive relationship between stability and the flow reversal depth that is consistent with the presence of blocked flow, though shallow events (<500 m) often occurred during unstable or neutral conditions as well. Deep down-valley flow also occurred in the presence of southerly low-level winds, with veering noted between 925 and 850 hPa during such events. As with stability, shallow down-valley flow occurred during a range of upstream wind directions without a preferred direction. Wind speed was not well-correlated with down-valley flow. Additionally, archived 1.33-km WRF-ARW model forecasts from OLYMPEX were analyzed in the context of environmental conditions, with results showing that WRF was capable of simulating down-valley flow and its antecedent/coincident conditions. Our analysis of environmental conditions showed that down-valley flow is most common during stable environments, southerly winds, and offshore pressure gradients—findings that were consistent with previous studies of down-valley flow (e.g., Colle and Mass 1996; Colle et al. 1999; Steiner et al. 2003; Bousquet and Smull 2006; Asencio and Stein 2006; Conrick et al. 2018; Zagrodnik et al. 2019) and conditions which are closely associated with the prefrontal sector of midlatitude cyclones (McMurdie et al. 2018).

Next, precipitation patterns were analyzed for each of the flow types. Data from two dozen rain gauges were used, most of which were located in and around the Quinault Valley. During deep down-valley flow, precipitation was enhanced along and near the Pacific Coast, with a decrease in precipitation noted within the Quinault Valley. Shallow down-valley flow was associated with lighter precipitation over the entire region. A particularly interesting feature associated with the observed precipitation pattern was the transition from positive precipitation anomalies along the coast to negative anomalies farther inland. While insufficient kinematic observations exist to elucidate a cause for these precipitation patterns, we hypothesize that lifting of air over the blocked upstream environment is at least partially responsible.

Finally, a case study of down-valley flow from OLYMPEX, the intense midlatitude cyclone of 16–17 November 2015, was analyzed using observations, reanalysis, and mesoscale model output. The first several hours of down-valley flow during the event were driven by the synoptic configuration and associated pressure gradient over the region. The second part of the event, however, was heavily influenced by an approaching warm front and its associated precipitation. To understand the role of latent cooling from evaporation and melting during this part of the event, we performed three simulations: 1) a Control simulation with all microphysical temperature tendencies enabled, 2) a simulation where melting does not contribute to the local temperature tendency (NoMelt), and 3) a simulation where evaporative cooling is turned off (NoEvap).

Evaporation was shown to be confined almost exclusively within the low-level reversed flow layer and, therefore, was hypothesized to have a larger impact than melting, which only briefly directly affected the reversed flow layer. Indeed, the

Brought to you by University of Washington Libraries | Unauthenticated | Downloaded 08/28/24 11:35 PM UTC

TABLE A1. Down-valley flow and environmental characteristics associated with the three classes of down-valley flow identified in the text. The final column provides information for periods when reverse flow was not detected at the DOW but precipitation was occurring. See section 3 for a description of parameters used to calculate the nondimensional mountain height.

	Deep down-valley flow, extending offshore	Deep down-valley flow, not extending offshore	Shallow down-valley flow	Nonexistent down-valley flow
No. of hours	97	74	57	57
Down-valley flow depth (km)	0.72 to 1.04	0.64 to 0.81	0.11 to 0.35	0
SEA–HQM pressure difference (hPa)	2.28 to 3.31	1.38 to 2.61	−0.62 to 1.21	−1.66 to −0.145
925-hPa wind direction (°)	150 to 164	160 to 200	193 to 245	230 to 264
925-hPa wind speed (m s^{-1})	12.82 to 20.66	10.15 to 16.62	9.68 to 17.23	11.85 to 18.97
850-hPa wind direction (°)	172 to 193	183 to 215	204 to 257	241 to 269
850-hPa wind speed (m s^{-1})	11.85 to 20.57	10.11 to 18.22	11.77 to 19.65	12.82 to 21.86
0.5–2.5-km mean N_m^2 ($\times 10^4$ s^{-1})	0.09 to 0.53	−0.14 to 0.27	−0.60 to −0.10	−0.39 to −1.71
Nondimensional mountain height	0.83 to 1.59	0.70 to 1.88	0.41 to 1.04	0.44 to 1.25

down-valley flow depth from the NoMelt simulation was nearly identical to that of the Control. In contrast, the NoEvap experiment simulated a faster end to the down-valley flow in the Quinault Valley. Further analysis showed that the removal of evaporative cooling warmed the lower levels of the atmosphere, which reduced low-level stability. Warmer temperatures also reduced the sea level pressure which allowed the simulated warm front to push into the Quinault Valley more rapidly. It was this combination of factors that was responsible for the earlier end of down-valley flow in the NoEvap simulation compared to the Control.

Our results highlight the complex relationships between the dynamics and thermodynamics during down-valley flow events, particularly when midlatitude cyclones make landfall. Many previous studies involving simulations (e.g., Asencio and Stein 2006; Zängl 2007) considered these effects to be acting separately, rather than in concert with one another. The 16–17 November 2015 case study showed that in the initial (prefrontal) stage of an approaching cyclone, both dynamic and thermodynamic effects can combine to favor deep down-valley flow. The transition to unblocked, onshore flow that followed the warm front passage was not associated with a rapid transition to up-valley flow but rather a gradual erosion of the down-valley flow layer as thermodynamic effects caused a shallow down-valley flow layer to persist for many hours beyond what would otherwise be expected based on the flow dynamics alone.

While we do recognize this study's limitations, such as restrictions to a single windward valley and case study, model resolution, and accuracy of model microphysics, this study offers an improved understanding of the complex nature of down-valley flow in the Quinault Valley, with implications beyond the Pacific Northwest.

Acknowledgments. The authors acknowledge Dr. Robert Houze for his early contributions to this work. This project was partially supported by funding from National Science Foundation Grants AGS-1657251 and AGS-2042105, and NASA Grant 80NSSC17K0279. The authors thank the Quinault Indian Nation, National Park Service, and National Forest Service for allowing the OLYMPEX project to install and operate the instrumentation on their lands. We also thank three anonymous reviewers and the editor, Prof. Justin Minder, whose comments greatly improved the manuscript.

Data availability statement. All data used in this manuscript are freely available at the following sources or by request from the corresponding author, including the following: WRF Model data, including namelists, are available upon request and will be made available via anonymous FTP. GFS forecast grids, used for initial/boundary conditions, are available from the National Centers for Environmental Information (NCEI) by visiting https://www.ncei.noaa.gov/products/weather-climate-models/global-forecast. NARR grids can be obtained through the NCEI at https://www.ncei.noaa.gov/products/weather-climate-models/north-american-regional. DOW radar data from OLYMPEX can be obtained via NASA at http://dx.doi.org/10.5067/GPMGV/OLYMPEX/DOW/DATA201. NPOL radar data form OLYMPEX can be obtained via NASA at http://dx.doi.org/10.5067/GPMGV/OLYMPEX/NPOL/DATA301.

APPENDIX A

Table of Down-Valley Flow Characteristics

The following table (Table A1) displays characteristics associated with each down-valley flow category, including periods of no down-valley flow. Except for the first row of data, which displays the number of hours of each flow category, each subsequent row provides the interquartile values associated with each category. Information about down-valley flow depth comes from the DOW radar, pressure data are from surface stations, and all other values are from NARR.

APPENDIX B

Model Evaluation

This appendix provides verification of WRF-ARW Model performance compared to NARR grids in order to build confidence in the results of down-valley flow simulations. First, we consider WRF performance during the November 2015 to January 2016 period considered in section 3 of this study.

Brought to you by University of Washington Libraries | Unauthenticated | Downloaded 08/28/24 11:35 PM UTC

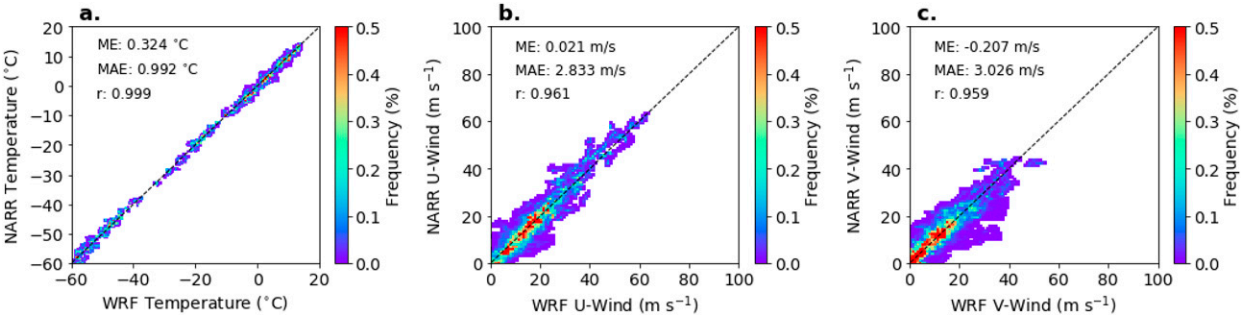

FIG. B1. Histograms of WRF-simulated meteorological conditions—(a) air temperature, (b) u-wind magnitude, and (c) v-wind magnitude—compared to conditions from the NARR dataset during the November 2015–January 2016 period.

WRF data for this period were from an archive of 6-h operational forecasts (initialized daily at 0000 UTC) from the OLYMPEX campaign. Only the innermost (1.33-km) domain was archived. We consider the 45 six-hour forecast grids that match with DOW times, as in the analyses performed in section 3. To facilitate comparisons, the NARR data are interpolated from its native ~32-km resolution to the WRF grid (1.33-km). WRF vertical coordinates are interpolated to match NARR pressure levels from 1000 to 100 hPa at 100-hPa increments.

Figure B1 shows histograms of air temperatures, east–west (u) wind magnitude, and north–south (v) wind magnitude from WRF and NARR. All three fields show good agreement, with low errors and high correlations exceeding 0.95. Temperature is best simulated by the WRF Model, though u- and v-wind fields exhibit similarly good agreement with the NARR, but with slightly larger variances. Figure B2 offers an evaluation of these fields in the context of their vertical distribution. As with Fig. B1, all three fields are consistent with one another. The only substantial deviation between the datasets is the low-level wind below 800 hPa, where WRF had slightly stronger wind speeds and u-wind at 200 and 300 hPa where NARR produced wind speeds slightly stronger than WRF.

For the case study analyzed in section 4, we also present an assessment of WRF accuracy as histograms of simulated environmental conditions compared with NARR grids at 6-h increments from 0600 UTC 16 November to 1800 UTC 17 November 2015. Data processing is the same as above. WRF output in Fig. B3 demonstrates the overall accuracy of WRF-simulated air temperatures, east-west (u) wind magnitude, and north-south (v) wind magnitude. Respective correlation coefficients

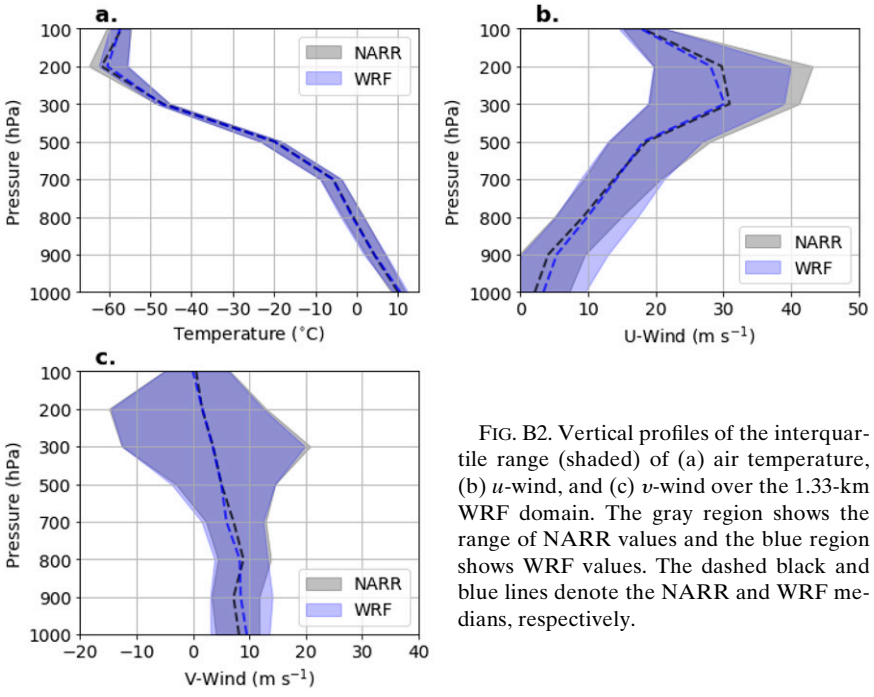

FIG. B2. Vertical profiles of the interquartile range (shaded) of (a) air temperature, (b) u-wind, and (c) v-wind over the 1.33-km WRF domain. The gray region shows the range of NARR values and the blue region shows WRF values. The dashed black and blue lines denote the NARR and WRF medians, respectively.

Brought to you by University of Washington Libraries | Unauthenticated | Downloaded 08/28/24 11:35 PM UTC

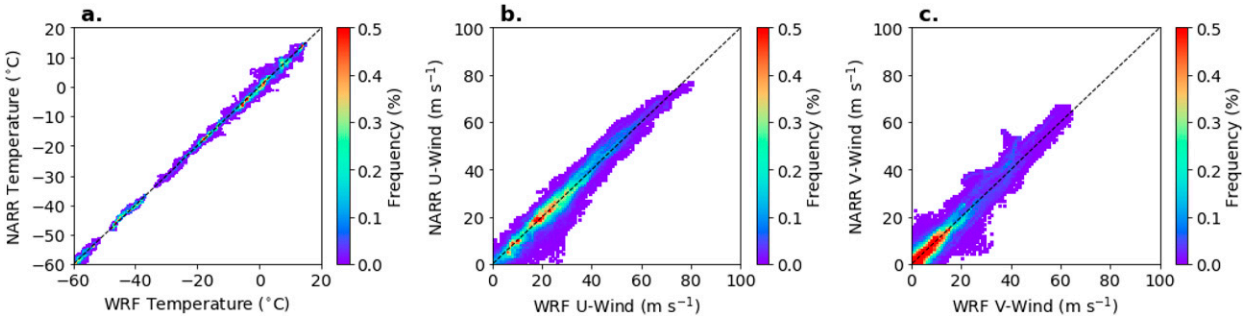

FIG. B3. Histograms of WRF-simulated meteorological conditions—(a) air temperature, (b) u-wind magnitude, and (c) v-wind magnitude—compared to conditions from the NARR dataset during the 16–17 Nov 2015 case study.

for simulated versus observed quantities are as follows: 0.991, 0.974, 0.973. Furthermore, mean errors (mean absolute errors) corresponding to air temperature, u-wind, and v-wind are as follows: 0.32 (0.82)°C, −0.20 (2.85) m s^{-1}, and 0.15 (2.57) m s^{-1}, respectively. This overview is indicative of an accurate WRF simulation that was capable of simulating the environmental conditions during the 16–17 November 2015 event.

REFERENCES

Asencio, N., and J. Stein, 2006: Origins of the reversed flow over the windward Alpine foothills during MAP IOP3 and IOP8. *Quart. J. Roy. Meteor. Soc.*, **132**, 297–316, https://doi.org/10.1256/qj.04.188.

Barnes, H. C., J. P. Zagrodnik, L. A. McMurdie, A. K. Rowe, and R. A. Houze Jr., 2018: Kelvin–Helmholtz waves in precipitating stratiform clouds of midlatitude cyclones. *J. Atmos. Sci.*, **75**, 2763–2785, https://doi.org/10.1175/JAS-D-17-0365.1.

Bond, N. A., and Coauthors, 1997: The Coastal Observation and Simulation with Topography (COAST) experiment. *Bull. Amer. Meteor. Soc.*, **78**, 1941–1955, https://doi.org/10.1175/1520-0477(1997)078<1941:TCOASW>2.0.CO;2.

Bougeault, P., and Coauthors, 2001: The MAP special observing period. *Bull. Amer. Meteor. Soc.*, **82**, 433–462, https://doi.org/10.1175/1520-0477(2001)082<0433:TMSOP>2.3.CO;2.

Bousquet, O., and B. Smull, 2003: Observations and impacts of upstream blocking during a widespread orographic precipitation event. *Quart. J. Roy. Meteor. Soc.*, **129**, 391–409, https://doi.org/10.1256/qj.02.49.

——, and ——, 2006: Observed mass transports accompanying upstream orographic blocking during MAP IOP8. *Quart. J. Roy. Meteor. Soc.*, **132**, 2393–2413, https://doi.org/10.1256/qj.05.103.

Carbone, R. E., W. A. Cooper, and W. C. Lee, 1995: Forcing of flow reversal along the windward slopes of Hawaii. *Mon. Wea. Rev.*, **123**, 3466–3480, https://doi.org/10.1175/1520-0493(1995)123<3466:FOFRAT>2.0.CO;2.

——, J. D. Tuttle, W. A. Cooper, V. Grubisic, and W. C. Lee, 1998: Trade wind rainfall near the windward coast of Hawaii. *Mon. Wea. Rev.*, **126**, 2847–2863, https://doi.org/10.1175/1520-0493(1998)126<2847:TWRNTW>2.0.CO;2.

Colle, B. A., and C. F. Mass, 1996: An observational and modeling study of the interaction of low-level southwesterly flow with the Olympic Mountains during COAST IOP 4. *Mon. Wea. Rev.*, **124**, 2152–2175, https://doi.org/10.1175/1520-0493(1996)124<2152:AOAMSO>2.0.CO;2.

——, ——, and B. F. Smull, 1999: An observational and numerical study of a cold front interacting with the Olympic Mountains during COAST IOP5. *Mon. Wea. Rev.*, **127**, 1310–1334, https://doi.org/10.1175/1520-0493(1999)127<1310:AOANSO>2.0.CO;2.

Conrick, R., and C. F. Mass, 2019: An evaluation of simulated precipitation characteristics during OLYMPEX. *J. Hydrometeor.*, **20**, 1147–1164, https://doi.org/10.1175/JHM-D-18-0144.1.

——, ——, and Q. Zhong, 2018: Simulated Kelvin–Helmholtz waves over terrain and their microphysical implications. *J. Atmos. Sci.*, **75**, 2787–2800, https://doi.org/10.1175/JAS-D-18-0073.1.

Durran, D. R., and J. B. Klemp, 1982: On the effects of moisture on the Brunt–Väisälä frequency. *J. Atmos. Sci.*, **39**, 2152–2158, https://doi.org/10.1175/1520-0469(1982)039<2152:OTEOMO>2.0.CO;2.

Grell, G. A., and S. R. Freitas, 2014: A scale and aerosol aware stochastic convective parameterization for weather and air quality modeling. *Atmos. Chem. Phys.*, **14**, 5233–5250, https://doi.org/10.5194/acp-14-5233-2014.

Hong, S. Y., Y. Noh, and J. Dudhia, 2006: A new vertical diffusion package with an explicit treatment of entrainment processes. *Mon. Wea. Rev.*, **134**, 2318–2341, https://doi.org/10.1175/MWR3199.1.

Hou, A. Y., and Coauthors, 2014: The Global Precipitation Measurement mission. *Bull. Amer. Meteor. Soc.*, **95**, 701–722, https://doi.org/10.1175/BAMS-D-13-00164.1.

Houze, R. A., Jr., C. N. James, and S. Medina, 2001: Radar observations of precipitation and airflow on the Mediterranean side of the Alps: Autumn 1998 and 1999. *Quart. J. Roy. Meteor. Soc.*, **127**, 2537–2558, https://doi.org/10.1002/qj.49712757804.

——, and Coauthors, 2017: The Olympic Mountains Experiment (OLYMPEX). *Bull. Amer. Meteor. Soc.*, **98**, 2167–2188, https://doi.org/10.1175/BAMS-D-16-0182.1.

——., J. Wurman, S. Brodzik, and A. Framback, 2018: GPM ground validation Doppler on Wheels (DOW) OLYMPEX V2. NASA Global Hydrometeorology Resource Center DAAC, accessed 1 July 2022, https://doi.org/10.5067/GPMGV/OLYMPEX/DOW/DATA201.

Iacono, M. J., J. S. Delamere, E. J. Mlawer, M. W. Shephard, S. A. Clough, and W. D. Collins, 2008: Radiative forcing by long-lived greenhouse gases: Calculations with the AER radiative transfer models. *J. Geophys. Res.*, **113**, D13103, https://doi.org/10.1029/2008JD009944.

James, C. N., and R. A. Houze Jr., 2005: Modification of precipitation by coastal orography in storms crossing northern

Brought to you by University of Washington Libraries | Unauthenticated | Downloaded 08/28/24 11:35 PM UTC

California. *Mon. Wea. Rev.*, **133**, 3110–3131, https://doi.org/10.1175/MWR3019.1.

Jiang, Q., 2003: Moist dynamics and orographic precipitation. *Tellus*, **55A**, 301–316, https://doi.org/10.3402/tellusa.v55i4.14577.

Klemp, J. B., 2011: A terrain-following coordinate with smoothed coordinate surfaces. *Mon. Wea. Rev.*, **139**, 2163–2169, https://doi.org/10.1175/MWR-D-10-05046.1.

Mass, C., and G. Ferber, 1990: Surface pressure perturbations produced by an isolated topographic barrier. Part I: General characteristics and dynamics. *Mon. Wea. Rev.*, **118**, 2579–2596, https://doi.org/10.1175/1520-0493(1990)118<2579:SPPPBA>2.0.CO;2.

McMurdie, L. A., A. K. Rowe, R. A. Houze Jr., S. R. Brodzik, J. P. Zagrodnik, and T. M. Schuldt, 2018: Terrain-enhanced precipitation processes above the melting layer: Results from OLYMPEX. *J. Geophys. Res. Atmos.*, **123**, 12 194–12 209, https://doi.org/10.1029/2018JD029161.

Medina, S., and R. A. Houze Jr., 2016: Kelvin-Helmholtz waves in extratropical cyclones passing over mountain ranges. *Quart. J. Roy. Meteor. Soc.*, **142**, 1311–1319, https://doi.org/10.1002/qj.2734.

Mesinger, F. G., and Coauthors, 2006: North American Regional Reanalysis. *Bull. Amer. Meteor. Soc.*, **87**, 343–360, https://doi.org/10.1175/BAMS-87-3-343.

Nakanishi, M., and H. Niino, 2006: An improved Mellor–Yamada level-3 model: Its numerical stability and application to a regional prediction of advection fog. *Bound.-Layer Meteor.*, **119**, 397–407, https://doi.org/10.1007/s10546-005-9030-8.

Niu, G.-Y., and Coauthors, 2011: The community Noah land surface model with multiparameterization options (Noah-MP): 1. Model description and evaluation with local-scale measurements. *J. Geophys. Res.*, **116**, D12109, https://doi.org/10.1029/2010JD015139.

Petersen, W. A., D. B. Wolff, J. Wang, and A. Tokay, 2017: GPM ground validation Met One rain gauge pairs OLYMPEX V1. NASA Global Hydrometeorology Resource Center DAAC, accessed 1 July 2022, https://doi.org/10.5067/GPMGV/OLYMPEX/GAUGES/DATA201.

Purnell, D. J., and D. J. Kirshbaum, 2018: Synoptic control over orographic precipitation distributions during the Olympics Mountains Experiment (OLYMPEX). *Mon. Wea. Rev.*, **146**, 1023–1044, https://doi.org/10.1175/MWR-D-17-0267.1.

Reinecke, P. A., and D. R. Durran, 2008: Estimating topographic blocking using a Froude number when the static stability is nonuniform. *J. Atmos. Sci.*, **65**, 1035–1048, https://doi.org/10.1175/2007JAS2100.1.

Rotunno, R., and R. Ferretti, 2003: Orographic effects on rainfall in MAP cases IOP 2b and IOP 8. *Quart. J. Roy. Meteor. Soc.*, **129**, 373–390, https://doi.org/10.1256/qj.02.20.

——, and R. A. Houze Jr., 2007: Lessons on orographic precipitation from the Mesoscale Alpine Programme. *Quart. J. Roy. Meteor. Soc.*, **133**, 811–830, https://doi.org/10.1002/qj.67.

Skamarock, W. C., and Coauthors, 2008: A description of the Advanced Research WRF version 3. NCAR Tech. Note NCAR/TN-475+STR, 113 pp., https://doi.org/10.5065/D68S4MVH.

Skofronick-Jackson, G., and Coauthors, 2017: The Global Precipitation Measurement (GPM) mission for science and society. *Bull. Amer. Meteor. Soc.*, **98**, 1679–1695, https://doi.org/10.1175/BAMS-D-15-00306.1.

Smith, R. B., 1980: Linear theory of stratified hydrostatic flow past an isolated mountain. *Tellus*, **32**, 348–364, https://doi.org/10.3402/tellusa.v32i4.10590.

Smolarkiewicz, P. K., and R. Rotunno, 1990: Low Froude number flow past three-dimensional obstacles. Part II: Upwind flow reversal zone. *J. Atmos. Sci.*, **47**, 1498–1511, https://doi.org/10.1175/1520-0469(1990)047<1498:LFNFPT>2.0.CO;2.

Steiner, M., O. Bousquet, R. A. Houze Jr., B. F. Smull, and M. Mancini, 2003: Airflow within major Alpine river valleys under heavy rainfall. *Quart. J. Roy. Meteor. Soc.*, **129**, 411–431, https://doi.org/10.1256/qj.02.08.

Thériault, J. M., and Coauthors, 2012: A case study of processes impacting precipitation phase and intensity during the Vancouver 2010 Winter Olympics. *Wea. Forecasting*, **27**, 1301–1325, https://doi.org/10.1175/WAF-D-11-00114.1.

——, J. A. Milbrandt, J. Doyle, J. R. Minder, G. Thompson, N. Sarkadi, and I. Geresdi, 2015: Impact of melting snow on the valley flow field and precipitation phase transition. *Atmos. Res.*, **156**, 111–124, https://doi.org/10.1016/j.atmosres.2014.12.006.

Thompson, G., and T. Eidhammer, 2014: A study of aerosol impacts on clouds and precipitation development in a large winter cyclone. *J. Atmos. Sci.*, **71**, 3636–3658, https://doi.org/10.1175/JAS-D-13-0305.1.

Whiteman, C. D., and J. C. Doran, 1993: The relationship between overlying synoptic-scale flows and winds within a valley. *J. Appl. Meteor.*, **32**, 1669–1682, https://doi.org/10.1175/1520-0450(1993)032<1669:TRBOSS>2.0.CO;2.

Wilson, T. H., and R. G. Fovell, 2018: Modeling the evolution and life cycle of radiative cold pools and fog. *Wea. Forecasting*, **33**, 203–220, https://doi.org/10.1175/WAF-D-17-0109.1.

Wolff, D., D. A. Marks, W. A. Petersen, and J. Pippit, 2017: GPM ground validation NASA S-Band Dual Polarimetric (NPOL) Doppler radar OLYMPEX V2. NASA Global Hydrometeorology Resource Center DAAC, accessed 1 July 2022, https://doi.org/10.5067/GPMGV/OLYMPEX/NPOL/DATA301.

Zagrodnik, J. P., L. A. McMurdie, and R. A. Houze Jr., 2018: Stratiform precipitation processes in cyclones passing over a coastal mountain range. *J. Atmos. Sci.*, **75**, 983–1004, https://doi.org/10.1175/JAS-D-17-0168.1.

——, ——, ——., and S. Tanelli, 2019: Vertical structure and microphysical characteristics of frontal systems passing over a three-dimensional coastal mountain range. *J. Atmos. Sci.*, **76**, 1521–154, https://doi.org/10.1175/JAS-D-18-0279.1.

——, L. McMurdie, and R. Conrick, 2021: Barrier and sub-barrier scale precipitation processes in high-resolution simulations of stratiform precipitation over the Olympic Mountains. *Mon. Wea. Rev.*, **149**, 503–520, https://doi.org/10.1175/MWR-D-20-0164.1.

Zängl, G., 2007: Reversed flow in the south-Alpine Toce Valley during MAP-IOP 8: Further analysis of latent cooling effects. *Quart. J. Roy. Meteor. Soc.*, **133**, 1717–1729, https://doi.org/10.1002/qj.155.

Brought to you by University of Washington Libraries | Unauthenticated | Downloaded 08/28/24 11:35 PM UTC